GRAIL-identified gravity anomalies in Oceanus Procellarum: Insight into subsurface impact and magmatic structures on the Moon

Ariel N. Deutsch[a], Gregory A. Neumann[b], James W. Head[a], Lionel Wilson[a,c]

[a]Department of Earth, Environmental and Planetary Sciences, Brown University, Providence, RI 02912, USA
[b]NASA Goddard Space Flight Center, Greenbelt, MD 20771, USA
[c]Lancaster Environment Centre, Lancaster University, Lancaster LA1 4YQ, UK

Corresponding author: Ariel N. Deutsch
Corresponding email: ariel_deutsch@brown.edu

Date of re-submission: 5 April 2019

Re-submitted to: *Icarus*
Manuscript number: ICARUS_2018_549

Highlights:

- Four positive Bouguer gravity anomalies are analyzed on the Moon's nearside.
- The amplitudes of the anomalies require a deep density contrast.
- One 190-km anomaly with crater-related topography is suggestive of mantle uplift.
- Marius Hills anomalies are consistent with intruded dike swarms.
- An anomaly south of Aristarchus has a crater rim and possibly magmatic intrusions.

Key words:
Moon; gravity; impact cratering; volcanism

Abstract

Four, quasi-circular, positive Bouguer gravity anomalies (PBGAs) that are similar in diameter (~90–190 km) and gravitational amplitude (>140 mGal contrast) are identified within the central Oceanus Procellarum region of the Moon. These spatially associated PBGAs are located south of Aristarchus Plateau, north of Flamsteed crater, and two are within the Marius Hills volcanic complex (north and south). Each is characterized by distinct surface geologic features suggestive of ancient impact craters and/or volcanic/plutonic activity. Here, we combine geologic analyses with forward modeling of high-resolution gravity data from the Gravity Recovery and Interior Laboratory (GRAIL) mission in order to constrain the subsurface structures that contribute to these four PBGAs. The GRAIL data presented here, at spherical harmonic degrees 6-660, permit higher resolution analyses of these anomalies than previously reported, and reveal new information about subsurface structures. Specifically, we find that the amplitudes of the four PBGAs cannot be explained solely by mare-flooded craters, as suggested in previous work; an additional density contrast is required to explain the high-amplitude of the PBGAs. For *Northern Flamsteed* (190 km diameter), the additional density contrast may be provided by impact-related mantle uplift. If the local crust has a density ~2800 kg/m^3, then ~7 km of uplift is required for this anomaly, although less uplift is required if the local crust has a lower mean density of ~2500 kg/m^3. For the *Northern* and *Southern Marius Hills* anomalies, the additional density contrast is consistent with the presence of a crustal complex of vertical dikes that occupies up to ~37% of the regionally thin crust. The structure of *Southern Aristarchus Plateau* (90 km diameter), an anomaly with crater-related topographic structures, remains ambiguous. Based on the relatively small size of the anomaly, we do not favor mantle uplift, however understanding mantle response in a region of especially thin crust needs to be better resolved. It is more likely that this anomaly is due to subsurface magmatic material given the abundance of volcanic material in the surrounding region. Overall, the four PBGAs analyzed here are important in understanding the impact and volcanic/plutonic history of the Moon, specifically in a region of thin crust and elevated temperatures characteristic of the Procellarum KREEP Terrane.

1. Introduction

The Oceanus Procellarum region of the northwest nearside of the Moon hosts four distinctive positive Bouguer gravity anomalies (PBGAs) (Evans et al., 2016): S*outhern Aristarchus Plateau*, *Northern* and *Southern Marius Hills*, and *Northern Flamsteed* (**Fig. 1**). These four PBGAs span a region ~700 km in N-S extent, and are all similar in gravitational amplitude (>140 mGal contrast) and shape (approximately circular in planform). The four PBGAs, which range between ~90 km and ~190 km in diameter (Table 1), can be distinguished due to their unique geologic settings (Section 2). These four spatially associated PBGAs are important in understanding the impact and volcanic/plutonic history of the nearside maria, in a region of anomalously thin crust (Wieczoreck et al., 2013) and elevated heat flow characteristic of the Procellarum KREEP Terrane (e.g., Warren and Wasson, 1979; Wieczorek and Phillips, 2000).

Analysis of gravity data is an excellent approach for characterizing the subsurface crustal and interior structure of a planetary body. For the Moon, the Gravity Recovery and Interior Laboratory (GRAIL) mission (Zuber et al., 2013a) has provided high-resolution gravity data that can provide constraints on the structure of the lunar interior. The vertical gradient of the GRAIL gravity potential, expanded from spherical harmonic degrees 6 to 600 on a sphere of radius 1738 km, is described here as the free-air gravity anomaly, analogous to terrestrial disturbances measured on an equipotential surface, or geoid. While nearly 98% of the power of the gravity signal at spherical harmonic degrees >80 correlates with topography, the remaining 2% cannot solely be explained by topography and contains important information about the interior and subsurface (Zuber et al., 2013b). The Bouguer gravity is corrected for the effects of topography assuming a constant density, and thus contains information about the subsurface. The very high resolution of the GRAIL data (Zuber et al., 2013a) approaches the scale of many geologic features, and with these data combined together, the interpretation of PBGAs can be made more confidently.

Here we explore six geologic endmember scenarios (**Fig. 2**) to model possible subsurface structures that may produce the four PBGAs (*Southern Aristarchus Plateau*, *Northern* and *Southern Marius Hills*, and *Northern Flamsteed*). The endmembers represent variations of lava-filled crater scenarios (e.g., Evans et al., 2016; Jozwiak et al., 2017; Baker et al., 2017) and variations of magmatic intrusion scenarios (e.g., Kiefer, 2013; Head and Wilson, 2017; Zhang et al., 2017). Previous works on the Marius Hills anomalies were restricted to lower resolution Lunar Prospector gravity data (Kiefer, 2013) and lower resolution GRAIL gravity data (Evans et al., 2016). Evans et al. (2016) estimated density contrasts of $850\frac{+300}{-200}$ kg/m^3 between the lunar crust and nearside maria. Here we explore a wide density contrast between 150 and 900 kg/m^3, and find that a smaller density contrast ~600 kg/m^3 may be more suitable for the sub-region in the mare that hosts the four PBGAs of interest (Section 3). Using our new modeling results from analysis of GRAIL data, we discuss regional impact and volcanic histories, and implications for the evolution of the lunar crust in the central Oceanus Procellarum region.

2. Geologic Setting

2.1. Southeast Aristarchus

The Aristarchus Plateau (AP), rising ~1.5 km above the surrounding Oceanus Procellarum, is characterized by a high incidence of volcanic features (Zisk et al., 1977; Whitford-Stark and

Head, 1977). Mare basalts, highland-type materials, and dark mantle materials interpreted to be pyroclastic deposits are all present in the AP (Zisk et al., 1977; Weitz et al., 1998; Mustard et al., 2011), and the plateau is incised by the largest sinuous rille on the Moon, Rima Schroeteri (Moore, 1965; Hurwitz et al., 2013). The variety and abundance of volcanic features within the AP indicate a complex volcanic history (Zisk et al., 1977; Jawin et al., 2016). To the southeast of the region is a ~100-km-diameter free-air gravity anomaly that peaks at ~166 mGal. This anomaly, referred to here as *Southern AP*, is characterized by a relatively smooth surface that has been flooded over by mare basalts (Hiesinger et al., 2011), distinguished only by some mare ridges and smaller, superposing impact craters (<~2 km in diameter). It has been proposed that a volcanic vent is located near the center of *Southern AP* at 21.44°N, -48.30°E (Stadermann et al., 2018), however it is also possible that the identified feature is an impact crater chain. The proposed vent does not appear to have any associated flows or flanks in topography data, and the circular features appear to have raised rims, which are more characteristic of impact craters than of volcanic craters (e.g., Zhang et al., 2016). Although no volcanic features are clearly visible on the surface of the *Southern AP* anomaly itself, it is possible that there are locally intruded features, especially given the abundance of volcanic features within the broader AP region (e.g., Zisk et al., 1977; Whitford-Stark and Head, 1977). Other crater structures, including smaller concentric craters (Trang et al., 2016) and sometimes lunar floor-fractured craters (FFCs) (e.g., Jozwiak et al., 2015), can display no extrusive volcanic features, however both of these crater types are explained by underlying magmatic intrusions. For Southern AP, it is also possible that any extruded features have been subsequently masked by mare flooding.

Previously, *Southern AP* has been suggested to be a buried impact crater due to the circularity of the positive Bouguer anomaly (Evans et al., 2016). This interpretation is consistent with a semi-circular topographic high present in topography data along the northern part of the anomaly at the edge of the AP, suggestive of a partial, ancient crater rim crest and wall.

2.2 Marius Hills

Marius Hills is the largest volcanic dome complex on the Moon, measuring 200 x 250 km across and consisting of nearly 300 cones and domes and 20 sinuous rilles (Whitford-Stark and Head, 1977; Whitford-Stark and Head, 1980; Head and Gifford, 1980; Stopar et al., 2010; Lawrence et al., 2013; Huang et al., 2013; Hurwitz et al., 2013; Huang et al., 2014; Head and Wilson, 2017; Zhang et al., 2017). While most domes and cones are less than 15 km across, individual structures reach 25 km across and rise to 500 m high (Whitford-Stark and Head, 1977; Srisutthiyakorn et al., 2010). This volcanic complex is of particular geologic interest because of the very high density of structures in the region; only ~200 additional volcanic domes have been identified elsewhere on the entire Moon (Head and Gifford, 1980). The maria in this region are primarily late Imbrian in age (~3.7 Ga), although some nearby maria date to possibly as young as 1.2 Ga (Hiesinger et al., 2003, 2011).

The free-air gravity anomalies at the northern and southern portion of the complex, referred to here as *Northern* and *Southern Marius Hills*, peaking at 145 mGal and 140 mGal respectively, have previously been investigated by other authors. For example, using Lunar Prospector data, Kiefer (2013) suggested that the anomalies are consistent with the presence of subsurface high-density basaltic dikes and sills, which served as magma chambers intruded into the porous feldspathic highland crust, and feeding the observed overlying surface volcanism. For *Northern Marius Hills* (centered at 14.0°N, 307.25°E), Kiefer (2013) suggested that a 160-km-diameter anomaly was caused by a 3.3-km-thick volcanic disk with a taper width of 25 km and mass of 2.1 x 10^{16} kg. The anomaly at *Southern Marius Hills* (8.25°N, 308.5°E) was suggested to have been caused by a 100-km-diameter, 12.9-km-thick volcanic disk, with a taper width of 20 km and disk mass of 2.9 x 10^{16} kg (Kiefer, 2013). Here, we revisit gravitational modeling of these anomalies with GRAIL data that have more than a six-fold higher spatial resolution than the Lunar Prospector data that he used.

Evans et al. (2016) analyzed GRAIL primary mission Bouguer gravity anomalies (filtered to degree and order 600) and suggested that the circular shapes of the PBGAs at Marius Hills may be consistent with buried impact craters, explained by the density contrast between the feldspathic crust and the subsequent infill of dense mare basalt. Zhang et al. (2017) considered the series of volcanic features associated with *Northern* and *Southern Marius Hills* and suggested that their morphologies are consistent with intruded sills beneath craters, concluding that impact craters (Evans et al., 2016) may produce crustal weakness zones that are favorable to the intrusion by sills and dikes. However, analysis of the genesis and evolution of magma on the Moon (e.g., Wilson and Head, 2017) suggests that magma is derived from depths of several hundreds of km and that shallow impact structures are unlikely to serve as direct conduits for ascending magma (Head and Wilson, 1991), except in the special case of FFCs (Jozwiak et al., 2012; Jozwiak et al., 2015; Wilson and Head, 2018), and there is no evidence of FFCs preserved at the surface for these particular anomalies. However, it is possible that surface evidence of FFCs has been masked by subsequent volcanism, and therefore we explore the possibility that these anomalies may be caused by buried FFCs later on in our analysis (Fig. 2).

GRAIL data are now available from both the primary and extended missions (Goossens et al., 2018). The solutions presented here from the sha.grgm1200b_rm1_1e1 model are of spherical harmonic degree 1200 windowed to degree 660 (Goossens et al., 2018), and are higher resolution than the solutions used by Kiefer (2013) (degree 110) and Evans et al. (2016) (degree 900 windowed to degree 600). With these new data, with an estimate of the density contrast between the crust in Marius Hills and mare basalts that is specific to this location, and with recent geologic analyses of the generation, ascent, and eruption of magma on the Moon (Head and Wilson, 2017; Wilson and Head, 2017), we are motivated to examine crustal density models in order to reevaluate the subsurface structures in the Marius Hills region.

2.3 Northern Flamsteed

The southernmost of the PBGAs in our analysis, *Northern Flamsteed,* coincides with topographic ridges trending northwest in the direction of Marius Hills, but is located ~300 km from the *Southern Marius Hills* anomaly. *Northern Flamsteed* is a broad ~178 mGal gravity anomaly that was identified by Frey (2011) as a quasi-circular crustal thickness anomaly in topography data derived from Clementine altimetry measurements and stereo images. He interpreted the *Northern Flamsteed* anomaly as a likely impact basin with a main ring diameter of 323 km. Frey (2011) discusses the strong contrast observed in the crustal thickness signature between the interior and exterior of the feature, and observe that the overall topography of this anomaly shows neither a partial rim structure nor an overall bowl-like depression. This anomaly, similar to the other three PBGAs in our analysis, was also identified as a buried crater in the database derived by Evans et al. (2016) using GRAIL data.

3. Methodology

3.1. Forward gravitational modeling

We use GRAIL gravity data (Zuber et al., 2013a), which at long wavelengths largely indicate variations in compensation state and thickness of the crust (Neumann et al., 1996; Wieczorek and Phillips, 1998; Wieczorek et al., 2013). The latest solutions from the GRAIL extended mission (e.g., GRGM1200B_RM1_1E1) use data from all altitudes in the primary mission (average altitude ~50 km) and the extended mission, which exploit satellite-to-satellite tracking at altitudes as low as 8 km in this region (average altitude ~28 km) to achieve maximum resolution of degree and order 1200 (Goossens et al., 2018). Spacing of ground tracks and small-scale density variations within the uppermost crust limit the increase in resolution and correlation with topography so we consider a maximum degree of 660, equivalent to ~8 km resolution, and discretize our forward models at roughly 2x2 km intervals. We remove the attraction of surface topography using the spherical harmonic expansion of Wieczorek and Phillips (1998), assuming a near-surface crustal density of 2800 kg/m^3 (Besserer et al., 2014) characteristic of the shallow nearside mare crust, to obtain Bouguer anomalies, which are evaluated at a reference radius of 1738 km. The Bouguer reduction value of 2800 kg/m^3 minimizes the background signal of smaller craters in the maria without affecting the amplitude of buried crater Bouguer anomalies (because they are buried and have no topographic correction). Regional admittance modeling for this region suggests that surface densities vary between 2750 kg/m^3 and 2900 kg/m^3 and decline with depth (Besserer et al., 2014); this indicates that the basaltic maria covering the surface are considerably denser than the average lunar highlands (bulk density of 2550 kg/m^3).

Neumann et al. (2018) solved for the best-fit Bouguer correction in the mare, border, and highlands in this region using preserved impact craters (i.e., craters that have not been obscured by any mare flooding). They find that the nearby highlands have an average crustal density of 2580 kg/m^3 and border materials are slightly denser, with a mean crustal density of 2700 kg/m^3. Craters in the mare themselves have a mean density of 3090 kg/m^3, but have a greater variance, and this may be due to differences in the thicknesses of mare layers overlying the less dense highlands crust (Neumann et al., 2018). The implication is that even at ~5 km depth, the mean density of the local mare is still relatively high (~3090 kg/m^3) (Neumann et al., 2018), and is likely to be higher than the ~2600 kg/m^3 density that is predicted by the estimated density gradient from Besserer et al. (2014). The mean density estimated for the mare (3090 kg/m^3) by Neumann et al. (2018) is similar to the bulk density estimated for the Marius Hills surface basalts (3150 kg/m^3) from Lunar Prospector Gamma Ray Spectrometer observations (Prettyman et al., 2006; Kiefer et al., 2012). In our analysis, we explore crustal densities from a lower endmember of 2500 kg/m^3 up to 2800 kg/m^3. The upper endmember crustal density is explored given that the best-fit Bouguer correction for well-preserved impact craters in this region approaches 3100 kg/m^3. As shown below, the crustal density employed for topographic correction has only a minor effect on the magnitude of the four Procellarum anomalies but exerts a major control on the structures and density contrasts used to interpret them.

We remove the longest wavelength variations in crustal structure, windowing the anomalies to spherical harmonic degrees 6-660 (corresponding to 8-km to 900-km half-wavelengths), and explore a range of infill and intrusion density contrasts between 150 and 900 kg/m^3, a range that includes the bulk density of 3150 kg/m^3 for the local maria (Kiefer et al., 2012) and the 2550 kg/m^3 bulk density of the average lunar highlands (Wieczorek et al., 2013). We model the anomalies, observe the residual gravitational disturbance, and discuss possible subsurface structures beneath the *Southern AP*, *Northern* and *Southern Marius Hills*, and *Northern Flamsteed* anomalies. Each subsurface structure is modeled as a ~2 km x 2 km discretized variation in relief on a surface representing a density contrast between crustal materials of varying composition at depth. The perturbations of gravity from shallow interfaces are regionally confined to distances not much greater than their depth when evaluated at the reference radius of 1738 km, while longer wavelength variations after the Bouguer correction are interpreted as variations in crustal thickness (Wieczorek et al. 2013).

Evans et al. (2016) previously analyzed quasi-circular mass anomalies within the lunar maria (including the four PBGAs studied here), and solved for density contrasts in high Bouguer anomaly craters of $850\frac{+300}{-200}$ kg/m^3 between the mare deposits and an underlying feldspathic crust, thought to be less dense than a global average of 2560 kg/m^3. Sood et al. (2017) modeled two circular Bouguer anomalies in mare regions revealed by gradiometry and argued that the anomalies were produced by infilling 160- to 200-km-diameter ancient craters by mare material with an excess density, taken as 640 kg/m^3, together with a component of mantle uplift. Because the Procellarum KREEP Terrane is relatively mafic (Kiefer, 2013) and partially buried craters in the study region such as Flamsteed P (Sood et al., 2017) often do not exhibit circular positive Bouguer anomalies, such an extreme density contrast as $850\frac{+300}{-200}$ kg/m^3 (Evans et al., 2016) is unlikely to apply to the four PBGAs in our study. Gravity inversions are necessarily non-unique and here we place limits on the thickness and relative density of post-impact mare-fill in buried impact craters. With localized solutions, we explore crust-mare density contrasts between 150 and 900 kg/m^3.

We model the density contrasts for each geologic endmember scenario as a series of cylinders with finite thicknesses. The mare outside of the proposed buried craters that is thinned by the presence of buried ejecta is modeled as negative topography, declining by a -3 power law from the height of the crater rim to a background level. We find models of best fit by varying cylinder parameters (Table 1) in order to qualitatively match our modeled gravity anomaly to the GRAIL-derived Bouguer gravity curve for each PBGA. All modeled cylinders are centered on the gravitational maximum of each anomaly. We find that we can model excellent fits to the four PBGAs with the adjustment of a small number of physical parameters (cylinder thickness, diameter, depth, density, and number). The total modeled gravity anomaly is the sum of the gravity from different subsurface load scenarios. The subsurface loads are uncompensated in these models, similar to the Kiefer (2013) models. The gravitational attraction of a finite-amplitude, discretized density interface is calculated at a radius of 1738 km, matching that of the Bouguer anomaly expansion, using the Cartesian frequency-domain expansion of Parker (1972) as implemented in the gravfft program of the Generic Mapping Tools software (Wessel et al., 2013). The effects of curvature are thus neglected, an approximation justified by the smaller-than-basin scale of the anomalies. Since the gravfft expansion does not preserve a regional mean value, the gravity disturbance calculated for each density interface is adjusted to reach a median value of zero over the ~1024 km × 1024 km model domain encompassing the four structures.

3.2. Analysis of geologic endmember scenarios

We consider six geologic endmembers (**Fig. 2**) when modeling various density contrast scenarios that may contribute to the GRAIL-derived PBGAs within central Oceanus Procellarum. The first scenarios are variations of lava-flooded impact craters: filled and buried impact craters (e.g., DeHon and Waskom, 1976; DeHon, 1979; Evans et al., 2016) (**Fig. 2.1**) and buried craters associated with mantle upwelling at the crust-mantle boundary (**Fig. 2.2**). We fill each crater with dense mare material, exploring density contrasts between 150 and 900 kg/m^3. For each PBGA, we estimate thicknesses in km for mare fill in a buried crater using a depth (d)-to-diameter (D) power-law relationship $d = 0.87\ D^{0.352}$ for fresh complex craters in the mare or $d = 1.558\ D^{0.254}$ for fresh complex craters in the lunar highlands derived from altimetry data (Kalynn et al., 2013) (**Table 1**). The diameters (D) of potential buried craters are estimated as the diameters of the anomalies from the gravity data, except for *Southern AP*, whose diameter is estimated from the preserved partial rim crest. The maximum thickness of the perturbing mare mass is the difference between the estimated depth of the relatively flat crater floor and the estimated depth of the surrounding terrain prior to flooding. We subtract the height of the crater rim (h), estimated using $h = 0.236\ D^{0.399}$ (Pike, 1977), which is modeled as a mass deficit (e.g., Sood et al., 2017) in an otherwise relatively uniform mare layer.

The d-to-D relationship established by Kalynn et al. (2013) was derived from topographic measurements of fresh complex lunar craters. However, the PBGAs studied here are much older, potentially Nectarian–Imbrian in age. Variations in target properties can have important differences on the impact crater morphology, and the subsurface temperature profile varies both with time and distance from the PKT (e.g., Miljković et al., 2013; 2016). Although some differences in complex crater morphometry may exist between the fresh (Eratosthenian and Copernican) craters studied by Kalynn et al. (2013) and the potentially Nectarian–Imbrian anomalies studied here, we do not account for such differences. Therefore, the thickness of mare infill for each anomaly derived from the estimated depth of each crater can be treated as a maximum value, given that the depth of potentially buried craters may be overestimated by the Kalynn et al. (2013) equation.

The remaining geologic endmembers are variations of subsurface magmatic intrusions: intruded sills or shallow magma reservoirs (Kiefer, 2013; Jozwiak et al., 2012, 2015, 2017; Wilson and Head, 2018) and concentrations of vertical dikes intruded in the subsurface (Head and Wilson, 2017; Head et al., 2018). We model these cases both with the presence of overlying filled impact craters (**Figs. 2.3–2.4**) and without the presence of filled impact craters (**Figs. 2.5–2.6**). The intrusions are modeled with mare-like densities between 3150 kg/m^3 and 3400 kg/m^3, resulting in a density contrast between the intrusions and surrounding crust ranging from 150 to 900 kg/m^3.

The gravitational modeling presented here represents different geologic endmembers, and of course countless variations of these scenarios could be modeled. Thus, our goal in this work is to provide endmember constraints on possible density structures beneath the four analyzed PBGAs. It is certainly possible that some of the anomalies may be best explained by some combination of the endmember scenarios presented here, such as some combination of intruded sills and dikes.

4. Results

4.1. Buried impact craters

Impact craters that are flooded by mare basalts can sometimes be identified by clear topographic signatures (e.g., preserved crater rim crests) or morphological characteristics (e.g., wrinkle ridge patterns) indicative of impact structure control. The expected topographic expression of filled impact craters depends on the level of mare fill that occurred post-impact. If minimal amounts of mare fill occurred such that the crater is not completely filled, then the crater rim crest should still be visible. If mare has filled to just over the top of the crater, then wrinkle ridges may be expected in the surrounding area (Lucchitta, 1977). However, if mare has completely flooded over the surface after the impact, then there may be no surface expression or geomorphology indicative of the presence of the now-buried impact crater. Some craters that have been completely buried by lava have been identified by gravity data (Neumann et al., 2015; Evans et al., 2016; Sood et al., 2017). PBGAs are generated from the density contrast between dense mare floods and the lunar crust (e.g., Neumann et al., 2015; Evans et al., 2016). These impact-related anomalies are typically circular due to the circular nature of the impact structures themselves (Neumann et al., 2015; Evans et al., 2016).

For each of the four PBGAs analyzed here, the thicknesses of the mare basalts are estimated as the difference in topography between the surrounding terrain and the impact crater floors; crater floor depths are estimated from *d*-to-*D* relationships (Kalynn et al., 2013). Using estimated mare thicknesses (Table 1), we first test the hypothesis that the four PBGAs are the expressions of basalt-filled, preexisting craters without substantial deformation of the crust-mantle interface (**Fig. 2.1**). **Fig. 3** shows that the amplitude of each GRAIL gravity anomaly cannot be approximated by modeling filled impact craters with a density contrast of either 350 kg/m^3 (resulting from a 2800 kg/m^3 crust and 3150 kg/m^3 mare fill) or 650 kg/m^3 (resulting from a 2500 kg/m^3 crust and 3150 kg/m^3 mare fill). We solve for the best-fit density contrasts for each anomaly (**Fig. 4**), and find that a density contrast between 730 and ~1040 kg/m^3 is required to match the peak amplitude of the circular anomalies if the thickness of mare fill is constrained by estimated mare basalt thicknesses from **Table 1**. The best-fit densities demonstrate that Model 1 (**Fig. 2.1**) is too simplistic because a crater fill requires an excessive density contrast. For example, *Northern AP* requires a density contrast of 1040 kg/m^3, which is unreasonable given that (1) this density contrast is much greater than what is predicted for a maximum endmember density contrast of 650 kg/m^3, estimated for a minimum crustal end-member (2500 kg/m^3) and the local mare flows (3150 kg/m^3), (2) there is no evidence for km-thick piles of surface mare flows in this region that could contribute additional density loading, and (3) this loading would require unrealistic crater geometries that are bowl-shaped and very deep, which is not supported by any crater modeling or surface observations. Thus, mare flooding of ancient impact craters alone (Evans et al., 2016) cannot adequately account for the amplitude of these gravity anomalies (**Fig. 3**).

However, the quasi-circular shapes of the four PBGAs are consistent with buried impact craters and have previously been discussed as such (Frey, 2011; Evans et al., 2016). The topography and geomorphology of these anomalies are also suggestive of impact structures (**Table 2**). *Southern AP* aligns with a partial, semi-circular topographic high (**Fig. 1**) that is consistent with an ancient crater rim crest, and the anomaly has a topographic low in the center, but does not exhibit a negative gravity anomaly associated with a buried rim crest. *Northern Marius Hills* is associated with linear rilles and graben proximal to the PBGA, which Zhang et al. (2017) suggested may indicate some impact structure control. However, there is no preservation of a rim crest, and the anomaly is located within an area of positive, not negative, topography. The topography of *Southern Marius Hills* is suggestive of a shallow depression (Zhang et al., 2017), where the overall relief is on the order of several hundred meters, and the anomaly coincides with curvilinear wrinkle ridges possibly consistent with a filled impact crater (**Fig. 1**). *Northern Flamsteed* shows a strong contrast between the interior and exterior of the anomaly in crustal thickness data (Frey, 2011). Finally, all four PBGAs appear as circular crustal thickness anomalies (**Fig. 5**) characterized by anomalously thin crust (<18 km) with respect to the regional crustal thickness (~34 km) (Wieczorek et al., 2013), suggestive of an impact origin. Given these various characteristics consistent with impact craters, we further explore the buried impact crater model, by coupling buried impact structures with mantle uplift (**Fig. 2.2**) (e.g., Baker et al., 2017).

The deep structures of lunar impacts have been studied through a combination of numerical impact modeling and topography and gravity observations. There is a morphological continuum from the smallest impact basins (protobasins) to the largest (peak-ring then multi-ring basins) (e.g., Melosh 1989; Baker et al., 2011; Osinski and Pierazzo, 2012). Numerical models demonstrate that the material in the central region of the crater is excavated and displaced during the basin-forming process, resulting in uplifted underlying mantle material, a central zone of thinned crust, and an annulus of thickened crust (e.g., Ivanov et al., 2010; Potter et al., 2012; Melosh et al., 2013; Miljković et al., 2013, 2015; Freed et al., 2014; Potter et al., 2015). Mantle uplift manifests in gravity data as positive anomalies due to the density contrast between the crust and the uplifted mantle. PBGAs have been observed regularly for basins > 200 km, and have been associated with some larger complex craters between ~150 and 200 km in diameter (Baker et al., 2017). The *Northern Flamsteed* anomaly (190 km) is within this diameter range and the remaining three PBGAs studied here are <150 km. However, this region of Oceanus Procellarum is characterized by anomalously thin crust (Wieczoreck et al., 2013) (**Fig. 5**), and the effects of preferential mantle uplift following impacts in this region have not been well-characterized in numerical studies. The crustal thicknesses estimated for the four PBGAs are between 14 and 18 km (**Table 1**), compared with a nearside average of 34 km (Wieczoreck et al., 2013).

Fig. 6 illustrates the results of our gravitational models for Model 2. For a crustal density of 2800 kg/m^3, coupling ~3–4 km of mare infill with ~5–7 km of mantle uplift produces the required density contrast to reach the amplitude of the GRAIL-derived Bouguer gravity for the four anomalies (**Fig. 6** brown solid line; **Table 1**). The density contrast trades off with both the amount of uplift and the geometry of the uplift, both of which are minimally constrained. If these two parameters are kept constant and the crust is modeled with a density of 2500 kg/m^3, then a positive Bouguer anomaly is produced that exceeds what is observed with GRAIL (**Fig. 6** brown dashed line; **Table 1**). Therefore, if the local crustal density beneath the analyzed PBGAs is more similar to ~2500 kg/m^3, then a smaller amount of mantle uplift beneath a buried impact crater could produce an anomaly similar to what is observed with GRAIL. In Section 5 we discuss whether it is likely for any of the PBGAs analyzed here to be related to impact structures and mantle uplift.

4.2. Subsurface magmatic intrusions beneath buried craters

Given the extensive variety and high spatial density of volcanic morphologies associated with the *Marius Hills* anomalies (the *Northern* has a considerably higher density than the *Southern*), we model how variations in magmatic intrusions may contribute to the observed gravity anomalies. For each intrusion scenario, we first maintain a buried impact crater in the model (**Figs. 2.3–2.4**) given (1) the quasi-circular shapes of these anomalies, (2) previous work suggesting these anomalies are buried craters (Evans et al., 2016), (3) some topographic features possibly suggestive of buried impact structures (**Table 2**), and (4) the circular crustal thickness anomalies suggestive of an impact origin (**Fig. 5**). Following these models, we explore magmatic intrusion scenarios without the presence of filled impact structures (Section 4.3).

Magmatic sills in the shallow subsurface can contribute to local density differences. However, such features are relatively infrequent on the Moon due to the low mean flux of lunar magma (Head and Wilson, 1992), the small percentage of lunar crust formed from mare basaltic magma (Head, 1976), and the resulting infrequency of dike emplacement (Head and Wilson, 1991). Sills tend to form when a dike encounters a low-density breccia lens prior to reaching equilibrium height (Wilson and Head, 2017). Dynamical analyses suggest that the rigidity change at the base of a breccia lens is likely to have initiated lunar sill injections, causing magma to flow horizontally to form an intrusion and raise the crater floor (Wilson and Head, 2018). Specifically, crater uplift on the order of several km can occur (Jozwiak et al., 2012, 2015), and the amplitude of sill inflation depends on the level the magma would have reached if the overlying structures were not present (Wilson and Head, 2017). An intrusive body in the shallow crust is expected to show topographic expression similar to that of a laccolith (Wilson and Head, 2017), as modeled by Michaut (2011), suggesting that smaller FFCs may show a domical uplift and larger craters, such as the complex craters considered here, may have intrusions with nearly uniform thickness and flatter floors (Jozwiak et al., 2012, 2015). Of the four PBGAs analyzed here, only *Northern Marius Hills* shows positive topographic relief. Additionally, FFCs are typically associated with concentric fractures (Jozwiak et al., 2012) and fracturing patterns are not observed at any of the four anomalies, although it is possible that such patterns were subsequently covered by mare fill.

Previous work statistically analyzing a group of FFCs demonstrated that PBGAs can be associated with FFCs (Thorey et al., 2015). However, analysis of Bouguer gravity solutions and individual FFCs revealed that Bouguer gravity anomalies are not a strong predictive tool for the presence of FFCs because shallow magmatic intrusions produce relatively low-amplitude Bouguer anomalies (Jozwiak et al., 2017). Jozwiak et al. (2017) surveyed a global catalog of FFCs (Jozwiak et al., 2012) and found that 52% of the observed craters are associated with positive central Bouguer anomalies, which are broadly correlated with the crater floors. They found that the identification of FFCs from Bouguer gravity is complicated by the coarse resolution of gravity data with respect to volcanic features and the dominance of mascons that can overpower the smaller signal of shallow magmatic intrusions. However, the use of band-filtered degree 100-600 gravity solutions revealed spatially heterogeneous Bouguer anomalies within FFCs (Jozwiak et al., 2017).

In this analysis we do not assess the four PBGAs at this band filter, but note that at degree 6-660, the four PBGAs appear concentrated and nearly circular in planform, exhibiting no characteristics of spatial heterogeneity (**Fig. 1**). It is possible that the four PBGAs studied here, postulated to be impact craters (Evans et al., 2016), are associated with shallow sills producing fracturing within the crater floor. However, if this were the case, it is clear that substantial mare flooding must have since occurred because no morphological features are seen that are suggestive of FFCs. The major gravitational signature in such a case is not likely to be dominated by the shallow intrusion (Jozwiak et al., 2017).

Nonetheless, it has previously been suggested that the *Marius Hills* anomalies are due to the presence of an intrusive sill in the shallow subsurface (**Fig. 2.3**) (Kiefer, 2013; Huang et al., 2013). To model this case, we first constrain our model with a 2-km thick sill intruded in the shallow subsurface (Table 1). Jozwiak et al. (2012) found that sill thicknesses range from ~0.14–2 km for the largest FFCs on the Moon. In **Fig. 7** we plot the resulting Bouguer anomaly for crustal densities of 2500 kg/m^3 (brown dashed lines) and 2800 kg/m^3 (brown solid lines), and for sill densities of 3150 kg/m^3 (denoted by the thinner lines) and 3400 kg/m^3 (denoted by the thicker lines). Even with an endmember density contrast of 900 kg/m^3 between the sills and crust, shallow 2-km thick volcanic sills beneath buried craters cannot account for the large, relatively compact PBGAs (**Fig. 7** thick brown dashed line). In fact, with a moderate density contrast of 350 kg/m^3, the sill thickness must exceed 10 km in order to fit the amplitude of the GRAIL-derived Bouguer anomaly. This is ~5x thicker than the predicted thicknesses of sills intruded beneath even the largest FFCs on the Moon (Jozwiak et al., 2012). If such a thick sill did exist, it would produce inflation, uplift, and fracturing associated with the anomalies (Jozwiak et al., 2012, 2015, 2017; Head and Wilson, 2017). Only the *Northern Marius Hills* anomaly exhibits positive topography, although no fracturing is observed. While it is unlikely that there is a single sill of this thickness, it is possible that the *Marius Hills* anomalies are due to a complex of multiple sills and dikes, whose cumulative thicknesses may be similar to ~10 km. It is easier to accommodate the loads of several layered smaller sills than to accommodate the load of a single unit on the flexural strength of the crust (Wichman and Schultz, 1995). However, recent analysis of country rock porosity and permeability in magmatic percolation and thermal annealing suggests that the densification of the crust via magmatic intrusions should result in crustal uplift. Given the lack of substantial uplift observed for these anomalies, we do not favor the presence of a single ~10 km-thick sill, or the presence of multiple sills whose cumulative thickness sum to ~10 km.

Kiefer (2013) discussed the possibility that a large volume of intruded material can be accommodated in the lunar crust with little changes in crustal volume through thermal annealing of the crustal host rock, which reduces the crustal porosity. Thermal annealing has been observed in some Apollo samples, most likely due to their proximity to impact melt (Cushing et al., 1999), although Kiefer (2013) suggested that intruded hot magma may also result in such annealing and that the positive topography associated with *Northern Marius Hills* may be due to the volume of intruded magma exceeding the volume of lost pore space (Kiefer, 2013). The process of material intruded during sill formation may have caused thermal annealing, porosity decrease, and country rock densification, and is very likely to have taken place at depth within the crust due to depth-dependent temperature profiles and enhanced heat flux in past thermal history, as described in detail by Wieczorek et al. (2013) and Besserer et al. (2014), who call on this effect to account for the closing of cracks with depth in the lower crust. Wieczorek et al. (2013) found that for the range of historical thermal gradients and viscosities, the minimum depth at which this effect would occur was ~40 km, below which cracks would be closed by thermal annealing effects. In a recent study following up on modeling the behavior of sill intrusions beneath floor-fractured craters (Wilson and Head, 2018), Head and Wilson (2019) assessed the role of thermal annealing in regions adjacent to sill-like intrusions in the upper crust. In a manner similar to, and consistent with, the findings of Wieczorek et al. (2013) for the deeper lunar crust, they found that even for crustal porosity values as high as 30%, the surface subsidence due to thermal annealing by a shallow sill intrusion would amount to only about 6% of the thickness of the sill (60 m for a 1-km thick sill). They concluded that for upper crustal sills, thermal annealing would indeed cause some densification, but that the magnitude of this effect is unlikely to significantly offset the density, gravity, and topographic effects of the sill intrusion itself (Head and Wilson, 2019). The intrusion of magma into cracks in the highlands crust was also treated quantitatively and found to be minimal (Head and Wilson, 2019).

Overall, the newer, higher resolution gravity data presented here have been used to model more accurately the density contrast of the Marius Hills anomalies. The presence of a large volume of intruded material in the form of a single dike is unfavored, given that *Southern Marius*

Hills is not associated with positive topography and that *Northern Marius Hills* is associated with only ~1 km of uplift. Our modeling suggests that some complex of intruded sills must sum to a ~10-km thick intrusion in order to fit the amplitude of the anomalies, and this thickness is not consistent with the lack of uplift observed.

Alternatively, it is possible that a swarm of dikes fed by a deep magma chamber is the source of the PBGAs (**Fig. 2.4**), and we find that this scenario can also provide enough density contrast to correspond to the GRAIL-derived signal (**Fig. 8**). In this scenario, a dike swarm is composed of dikes that penetrate vertically to the surface, as well as some that stall in the crust. If sufficiently pervasive, this plexus of dikes could contribute to a positive gravitational signature. Head and Wilson (1992) suggested that the upper limit for the fraction of global crust occupied by dikes is 37–50% by volume. An estimated upper limit for the intrusion to extrusion ratio for the global crust is ~50:1, but the ratio may be considerably less, or perhaps even enhanced at local volcanic complexes (Head and Wilson, 1992).

The various individual dikes can be combined to be modeled as a single cylinder following the principles of linear combinations. We vary the crustal volume occupied by dikes (Wilson and Head, 1992) in order to estimate the amount of subsurface, high-density material that can produce four PBGAs. For a crustal density of 2800 kg/m^3, modeling the amplitudes of the four GRAIL-derived gravity anomalies requires a cylinder of dikes with density contrasts between ~225 and 300 kg/m^3, filling ~37 to 50% of the crustal volume to a depth of ~19 km, which is the average depth of the crust-mantle boundary in this region (**Fig. 8**).

More magma is likely to be intruded in the lower crust than what is accounted for by the magmas that reached the surface (Head and Wilson, 1992). While the ratio of intruded to extruded material in the lunar crust is unknown, geophysical models suggest that the ratio may be as great as 50:1 (Head and Wilson, 1992). Such high volumes of intruded material may be predicted to produce substantial displacement and, subsequently, surface deformation features, but there are no major deformation features related to crustal displacement observed in the Marius Hills region. One of the major findings of the GRAIL mission was that the lunar crust is relatively porous (Wieczorek et al., 2013; Besserer et al., 2014), and an average crustal porosity of 12% was derived for the Moon (Wieczorek et al., 2013). Wieczorek et al. (2013) predicted that pore closure within the Moon may occur between 40 and 85 km below the surface; thus porosity could exist in the underlying mantle in our study region, where the average crustal thickness is ~35 km. When magma overpressurization causes sufficient stress and subsequent brittle deformation of the elastic lithosphere, a dike propagates toward the surface (Head and Wilson, 2017). Thermal evolution models of the lunar interior suggest that the elastic lithosphere was between 100 and 150 km thick during the major period of mare volcanism between 3 and 4 Ga (e.g., Solomon and Head, 1980; Hess and Parmentier, 2001; Wieczorek et al., 2006; Shearer et al., 2006). During the waning stages of an eruption, the effusion rate decreases and dike closure occurs, allowing for relaxation of the intruded structures (Head and Wilson, 2017).

The presence of dikes is indeed required to feed the mare basalt deposits observed at the four sites. Furthermore, the presence of multiple dikes in the Marius Hills is consistent with the volcanic morphologies in this region (Lawrence et al., 2013; Head and Wilson, 2017), and the analysis of generation, ascent, and eruption of mare basalts (Head and Wilson, 2017). Higher-flux eruptions may produce the observed sinuous rilles, and the morphologies of individual domes may be explained by low effusion-rate eruptions producing cooling-limited flows, representing the final stages of dike closure (Lawrence et al., 2013; Head and Wilson, 2017). Head and Wilson (2017) estimate that at least 10 large-volume dikes are required to feed the

~10,000 km^3 Marius Hills complex, which is consistent with this model of multiple dikes being fed by a large, long-lived but currently solidified diapiric source region in the mantle. Here we assume that the source region is located at a neutral buoyancy depth, having cooled and having reached the same density as the surrounding mantle.

Overall, we support the conclusion of Kiefer (2013) that the *Northern* and *Southern Marius Hills* anomalies require a substantial volume of subsurface, high-density material. Our gravitational models find that the presence of a mare-filled crater coupled with either multiple sills (summing to ~10 km in thickness) or the presence of a dense vertical dike swarm is consistent with the amplitude of the GRAIL-derived anomalies. From the gravitational modeling alone, it is not possible to discern between these two (or other) scenarios. However, on the basis of studies of magmatic intrusion-related processes in the lunar crust (Head and Wilson, 2019), the presence of subsurface sills is not favored.

4.3 Subsurface magmatic intrusions without buried craters

We also consider these magmatic intrusion scenarios without the presence of flooded craters (**Figs. 2.5–2.6**). Because the amplitude of the GRAIL-derived Bouguer anomaly could not be matched in even the maximum endmember case (density contrast of 900 kg/m^3) for Model 3, we do not model the specific case in which subsurface sills are intruded beneath each PBGA and there are no overlying buried impact craters.

Fig. 9 shows the results for Model 6, in which vertical dike swarms are not overlain by buried impact structures, and therefore the dikes propagate from the crust-mantle boundary to the shallow subsurface and surface. In **Fig. 9**, the blue profiles represent the Bouguer modeled anomalies predicted for dikes that occupy 37% of the lunar crust, and the red profiles represent the anomalies predicted for dikes that occupy 50% of the crust, all for a crustal density of 2500 kg/m^3 (dashed lines) and 2800 kg/m^3 (solid lines). Without the presence of a mare-filled crater, the four anomalies require a 2800 kg/m3 crust to be occupied by at least ~37% dikes (blue solid line), and <37% of a 2500 kg/m3 crust can be occupied by dikes and produce anomalies similar in amplitude to what is observed by GRAIL (blue dashed line) (Table 1).

In conclusion, we favor the explanation that the *Southern Marius Hills* anomaly is caused by a flooded impact crater and the presence of subsurface dikes or multiple sills because of its circular topographic low suggestive of an impact structure. In contrast, the topography and morphology of *Northern Marius Hills* is not indicative of an impact crater. We find that the amplitude of the GRAIL-derived anomaly can be fit by models of either a subsurface dike complex, or a subsurface dike complex coupled with a flooded crater. We cannot rule out the possibility that the geometries of subsurface dikes have produced a circular anomaly and that *Northern Marius Hills* is due to intruding dikes alone. Although there is no impact-related topography present, it is possible that impact-related features are hidden by the extensive mare flooding.

5. Discussion

5.1. Impact cratering in central Oceanus Procellarum

Evans et al. (2016) identified more than 100 quasi-circular Bouguer gravity anomalies between 26 and 300 km in diameter, located within and near the nearside maria, four of which are the PBGAs studied here. They suggested that the majority of the identified PBGAs are impact craters that have been buried by mare basalt and/or impact ejecta. Evans et al. (2016) supported this conclusion by the observations that (1) the most widespread, quasi-circular features on the Moon are impact craters, (2) the population of gravity anomalies can be subdivided into one group characterized by large PBGAs consistent with mare-filling and a second group characterized by small negative Bouguer gravity anomalies consistent with impacts into mare deposits, both of which are observed for partially filled lunar craters (Zuber et al., 2013a), and (3) similarly sized craters of volcanic origin (calderas) have not been observed on the Moon (Head and Wilson, 2017) and are not favored under magma generation, ascent, and eruption conditions (Head and Wilson, 1991).

Here we support the conclusion of Evans et al. (2016) that *Southern AP*, *Northern* and *Southern Marius Hills*, and *Northern Flamsteed* are likely to be buried and filled impact craters. However, our results suggest that these four PBGAs cannot be explained by mare fill alone; an additional density contrast is required in order to model the large amplitude of these PBGAs (**Table 1**; **Fig. 3; Fig. 4**). For both *Marius Hills* anomalies, which exhibit a variety of volcanic features on their surfaces, it is plausible that this additional density contrast may be provided either by a complex of multiple intruded sills (**Fig. 7**), or subsurface dikes intruding into the crust (**Fig. 8**). While *Southern AP* is not associated with any surface volcanic features other than the maria themselves, it is located adjacent to the broader *AP* region, which is characterized by a high spatial density of volcanic features (e.g., Zisk et al., 1977; Whitford-Stark and Head, 1977). It is possible that any other extrusive features were covered by the maria themselves, and that locally intruded features exist. Thus, the additional density contrast for *Southern AP* may also be of magmatic origin.

As with the other anomalies, it is possible that *Northern Flamsteed* may have locally intruded features contributing to its high-amplitude positive anomaly. But in contrast to the other three PBGAs, *Northern Flamsteed* is not coincident within any volcanic complexes, and volcanic features associated with this anomaly are restricted to maria and ridges. Therefore, we consider an alternative possibility to explain the additional density contrast required to fit the amplitude of the gravity anomaly: mantle uplift. In Section 4.1, we found that the amplitude of the anomaly could be well-approximated by buried craters associated with mantle upwelling (**Fig. 6**).

The relationship between gravity anomalies and the structures of lunar impact features has previously been studied. For example, peak-ring basins (PRBs) (>~200 km in diameter) are characterized by a central positive Bouguer anomaly within the peak ring and a negative Bouguer gravity annulus extending to near the basin rim crest (Neumann et al., 1996; 2015; Namiki et al., 2009; Baker et al., 2017). These gravity anomalies are interpreted as being due to mantle uplift within the peak ring and the presence of an annulus of thickened crust between the peak ring and the basin rim crest (**Fig. 10**). The four PBGAs that we study are unlikely to be PRBs because there is no evidence of basin-scale structures in the topography or morphology (**Fig. 1**) suggestive of outer rings. Additionally, the estimated crustal thicknesses associated with the four PBGAs are suggestive of anomalously thin crust that correlates with the PBGAs, but no annulus of thickened crust (**Fig. 5**).

Baker et al. (2017) statistically analyzed a large (*N*=968) sample of impact structures and found that some larger complex craters between ~150 and 200 km in diameter are characterized by PBGAs. They found that PBGAs begin to dominate for impact craters with diameters of ~150 km, while a negative annulus signal begins at diameters of ~200 km, near the onset of PRBs. Therefore, the highly irregular nature of Bouguer anomalies associated with complex craters may represent the transition in impact structure morphology between complex craters and PRBs (Baker et al., 2017). The statistical analysis of Baker et al. (2017) is consistent with numerical impact studies by Milbury et al. (2015), who modeled the formation of lunar impact structures. Milbury et al. (2015) found that Bouguer anomalies are primarily controlled by the preimpact porosity until a crater diameter of ~140 km, and then by mantle uplift beyond a crater diameter of 215 km. *Northern Flamsteed* is ~190 km in diameter, and thus fits well within the diameter range analyzed by both Baker et al. (2017) and Milbury et al. (2015) for which mantle uplift begins to occur. With PBGAs of this size (~190 km), surrounding negative Bouguer anomalies are not observed (Baker et al., 2017) (**Fig. 10**). Importantly, numerical modeling also suggests that mantle uplift cannot explain the PBGA of relatively smaller impact structures (Milbury et al., 2015), such as the *Marius Hills* or *Southern AP* anomalies studied here.

In general, smaller impactors excavate and displace less target material, resulting in less mantle uplift during the collapse of the transient crater (e.g., Melosh et al., 2013). The diameter of the *Southern AP* anomaly is only ~100 km, which is smaller than the diameter of impact structures for which PBGAs are typically observed (Baker et al., 2017). Miljković et al. (2016) numerically modeled the formation of lunar impact basins using the iSALE-2D hydrocode and found that for crustal thinning diameters <~200 km, the models cannot reproduce observed mantle uplift structures. Similarly, Potter (2012) simulates impacts traveling 10 km/s and 15 km/s into a 60 km-thick crust and finds that, though the results are highly dependent on the thermal profile, basins typically begins to uplift mantle material to the lunar surface at an annulus radius $\gtrsim$200 km.

However, as mentioned earlier, all four anomalies are located in a region where the crust is anomalously thin (Wieczorek et al., 2013), which may provide a setting more conducive to mantle uplift in response to the impact cratering process. For example, numerical simulations by Miljković et al. (2016) demonstrate that mantle exposures occur most commonly for impacts in the thinnest crust (~30 km), which is even thicker than the ~16 km-thick crust local to the anomalies analyzed here. In general, more modeling is required to understand the specific impact response for craters between ~100 and 200 km in ~16-km thick crust.

In conclusion, numerical impact simulations do not support the hypothesis that a relatively small impact structure, such as *Southern AP*, may have considerable mantle uplift. The gravitational model presented in **Fig. 6** is of course a non-unique solution, and any fit to the GRAIL-derived signal does not guarantee the correctness of the modeled geologic scenario. For the *Southern AP* anomaly, it is possible (and perhaps more likely, as discussed above) that the observed flooded crater is coupled with intrusive materials.

5.2. Topographic expression of the PBGAs

While *Southern AP*, *Southern Marius Hills*, and *Northern Flamsteed* are associated with topography and surface morphology suggestive of filled and buried impact craters (**Table 2**), *Northern Marius Hills* exhibits hundreds of meters of positive relief relative to the surrounding mare surface. The high topography at *Northern Marius Hills* has previously been explained as being due to a substantial volume (~1.6×10^4 km^3) of intruding subsurface basalt uplifting the surface (Kiefer, 2013). We find that a ~10-km thick sill is required to fit the observed Bouguer gravity anomaly at *Northern Marius Hills* (**Table 1**) at a density contrast of 350 kg/m^3. The presence of a single ~10-km thick sill is unreasonable given that sills beneath the largest FFCs on the Moon are estimated to be <2 km thick (Jozwiak et al., 2012), and the presence of a complex of multiple sills and dikes, whose cumulative thicknesses sum to ~10 km, is not favored given that substantial uplift is expected (e.g., Head and Wilson, 2019) but not observed.

Positive topography at *Northern Marius Hills* may alternatively be explained by a constructional complex of small shield volcanoes (e.g., Whitford-Stark and Head, 1977; Spudis, 1996). Small shield volcanoes on the Moon often have summit craters, and are low, convex-upward, quasi-circular structures with slopes <5°, formed from relatively low effusion rates of cooling-limited flows (Head and Gifford, 1980; Tye and Head, 2013; Head and Wilson, 2017). Small shields are constructed from a succession of eruptions, early ones having high eruption rates resulting in broad, long lava flows, and subsequent eruptions with lower effusion rates, producing cooling-limited flows that do not advance far from the vent (Head and Wilson, 2017). The construction of compound flow fields occurs through the ponding, inflation, and superposition of flows, resulting in the vertical accumulation of flows (Whitten and Head, 2013). The accretion of small volcanic edifices and compound flow fields is consistent with the topography of Marius Hills (Tye and Head, 2013).

6. Conclusions

The GRAIL nominal and extended mission data (Goossens et al., 2018) analyzed and discussed here permit higher resolution gravity modeling than in previous studies (e.g., Kiefer et al., 2013; Evans et al., 2016). These data demonstrate that the amplitude of the four PBGAs cannot be explained by mare-filled craters alone, as inferred by Evans et al. (2016), and instead require an additional density contrast. Coupled with geologic analyses, our modeling suggests that this density contrast can be explained by two reasonable geometries:

(1) First, 5–7 km of mantle uplift (ρ = 3400 kg/m^3) combined with 3–4 km of mare fill (ρ = 3150 kg/m^3) in impact craters (**Fig. 2.2**) provide a good fit to the GRAIL-derived signals (**Fig. 6**) for a local crustal density of 2800 kg/m^3. Less uplift is required if the local crust has a lower mean density of 2500 kg/m^3. The anomalously thin crust in this region of Oceanus Procellarum (Wieczorek et al., 2013; **Fig. 5**) may provide more favorable conditions than the average lunar crust for mantle upwelling in response to cratering events of the size of the PBGAs (Miljković et al., 2016). We favor this mantle upwelling scenario for the *Northern Flamsteed* anomaly (190 km), which is within the transitional size range between complex craters and peak-ring basins.

(2) Alternatively, subsurface magmatic material can also provide the necessary density contrast in order to correspond to the amplitude of the GRAIL-derived anomalies. In the case where subsurface sills are present, a cumulative thickness of ~10 km is required. Given the lack of extreme (km's-worth) of uplift for these anomalies, we do not favor this case. In the case where a vertical dike complex in the crust is fed by a long-lived diapiric source region, a plexus of dikes is modeled as a single cylinder that occupies up to 50% of the lunar crust beneath each anomaly. The two PBGAs associated with the Marius Hills volcanic complex can be well-approximated by a dike complex extending from the crust-mantle boundary to the floors of mare-filled impact craters (Model 4) (**Fig. 8**), or by a dike complex extending from the crust-mantle boundary to the surface, without the presence of filled impact craters (Model 6) (**Fig. 9**). We favor the presence of filled craters at both locations due to these PBGAs aligning with circular crustal thickness anomalies suggestive of an impact origin (**Fig. 5**). In addition, impact-related topographic signatures are observed at *Southern Marius Hills*. The *Northern Marius Hills* anomaly is

not associated with impact-related topography; however, it is possible that extensive flooding has erased the surface expression of any impact structures that once existed. In both Model 4 and Model 6, a network of subsurface dikes fed by a deep mantle reservoir is consistent with the variety and density of volcanic morphologies on the surface (Head and Wilson, 2017).

The source of the *Southern AP* anomaly remains ambiguous and its magnitude can be well approximated by either of these additional density contrasts. Based on the anomaly's diameter (~100 km), mantle uplift is not predicted by previous analyses (e.g., Baker et al., 2017). However, the mantle response in a region of especially thin crust needs to be better resolved. *Southern AP* may also be due to a vertical dike complex (**Fig. 8** or **Fig. 9**) given the high density of volcanic material in the surrounding region.

Acknowledgements

We thank Walter Kiefer and one anonymous reviewer for their helpful reviews of this work, and Francis Nimmo for his editorial handling of this manuscript. We also thank Alexander Evans for helpful discussions about this work. This work is supported by NASA under grant number NNX16AT19H issued through the Harriett G. Jenkins Graduate Fellowship to A.N.D., by the Discovery Program to G.A.N., by the Solar System Exploration Research Virtual Institute to J.W.H., by the Leverhulme Trust to L.W. through an Emeritus Fellowship, and by the LRO LOLA team through grant number NNX09AM54G to J.W.H.

References

Baker, D.M.H., Head, J.W., Neumann, G., Smith, D.E., Zuber, M., 2012. The transition from complex craters to multi-ring basins on the Moon: Quantitative geometric properties from Lunar Reconnaissance Orbiter Lunar Orbiter Laser Altimeter (LOLA). J. Geophys. Res. Planets 117, E00H16. https://doi.org/10.1029/2011JE004021.

Wilson, L., Head, J.W., 2002. Tharsis-radial graben systems as the surface manifestation of plume-related dike intrusion complexes: Models and implications. J. Geophys. Res. Planets 107, 1–1. https://doi.org/10.1029/2001JE001593.

Baker, D.M.H., Head, J.W., Neumann, G., Smith, D.E., Zuber, M., 2012. The transition from complex craters to multi-ring basins on the Moon: Quantitative geometric properties from Lunar Reconnaissance Orbiter Lunar Orbiter Laser Altimeter (LOLA). J. Geophys. Res. Planets 117, E00H16. https://doi.org/10.1029/2011JE004021.

Baker, D.M.H., Head, J.W., Phillips, R.J., Neumann, G.A., Bierson, C.J., Smith, D.E., Zuber, M.T., 2017. GRAIL gravity observations of the transition from complex crater to peak-ring basin on the Moon: Implications for crustal structure and impact basin formation. Icarus 292, 54–73. https://doi.org/10.1016/j.icarus.2017.03.024.

Besserer, J., Nimmo, F., Wieczorek, M.A., Weber, R.C., Kiefer, W.S., McGovern, P.J., Andrews-Hanna, J.C., Smith, D.E., Zuber, M.T., 2014. GRAIL gravity constraints on the vertical and lateral density structure of the lunar crust. Geophys. Res. Lett. 41, 5771–5777. https://doi.org/10.1002/2014GL060240.

Çushing, J.A., Taylor, G.J., Norman, M.D., Keil, K., 1999. The granulitic impactite suite: Impact melts and metamorphic breccias of the early lunar crust. Meteoritics & Planetary Science 34, 185–195. https://doi.org/10.1111/j.1945-5100.1999.tb01745.x.

DeHon, R.A., 1979. Thickness of the western mare basalts. Proc. Lunar Planet. Sci. Conf. 10, 2935–2955.

DeHon, R.A., Waskom, J.D., 1976. Geologic structure of the eastern mare basins. Proc. Lunar Sci. Conf. 7, 2729–2746.

Evans, A.J., Soderblom, J.M., Andrews-Hanna, J.C., Solomon, S.C., Zuber, M.T., 2016. Identification of buried lunar impact craters from GRAIL data and implications for the nearside maria. Geophys. Res. Lett. 43, 2015GL067394. https://doi.org/10.1002/2015GL067394.

Freed, A.M., Johnson, B.C., Blair, D.M., Melosh, H.J., Neumann, G.A., Phillips, R.J., Solomon, S.C., Wieczorek, M.A., Zuber, M.T., 2014. The formation of lunar mascon basins from impact to contemporary form. J. Geophys. Res. Planets 119, 2378–2397. https://doi.org/10.1002/2014JE004657.

Frey, H., 2011. Previously unknown large impact basins on the Moon: Implications for lunar stratigraphy, in: Geological Society of America Special Papers. Geological Society of America, 53–75. https://doi.org/10.1130/2011.2477(02).

Goossens, S.J., Sabaka, T.J., Wieczorek, M., Neumann, G.A., Lemoine, F.G., Mazarico, E.M., Smith, D.E., Zuber, M.T., 2018. High-resolution gravity field models from GRAIL data and implications for the density structure of the Moon's crust. American Geophysical Union Fall Meeting, abstract #409568.

Head, J.W., 2010. Lunar volcanism in space and time. Reviews of Geophysics 14, 265–300. https://doi.org/10.1029/RG014i002p00265.

Head, J.W., et al., 2018, *in review*. Marius Hills volcanic complex: Generation, ascent and eruption of magma in a thin crustal, high heat flux environment.

Head, J.W., Gifford, A., 1980. Lunar mare domes: Classification and modes of origin. The Moon and the Planets 22, 235–258. https://doi.org/10.1007/BF00898434.

Head, J.W., Wilson, L., 1991. Absence of large shield volcanoes and calderas on the Moon: Consequence of magma transport phenomena? Geophys. Res. Lett. 18, 2121–2124. https://doi.org/10.1029/91GL02536.

Head, J.W., Wilson, L., 1992. Lunar mare volcanism: Stratigraphy, eruption conditions, and the evolution of secondary crusts. Geochimica et Cosmochimica Acta 56, 2155–2175. https://doi.org/10.1016/0016-7037(92)90183-J.

Head, J.W., Wilson, L., 2017. Generation, ascent and eruption of magma on the Moon: New insights into source depths, magma supply, intrusions and effusive/explosive eruptions (Part 2: Predicted emplacement processes and observations). Icarus 283, 176–223. https://doi.org/10.1016/j.icarus.2016.05.031.

Head, J.W., Wilson, L., 2019. Dike intrusion-related processes in the lunar crust: The role of country rock porosity/permeability in magmatic percolation and thermal annealing, and implications for gravity signatures. 10th MS-3, abstract.

Hiesinger, H., Head, J.W., Wolf, U., Jaumann, R., Neukum, G., 2003. Ages and stratigraphy of mare basalts in Oceanus Procellarum, Mare Nubium, Mare Cognitum, and Mare Insularum. J. Geophys. Res. Planets 108. https://doi.org/10.1029/2002JE001985

Hiesinger, H., Head, J.W., Wolf, U., Jaumann, R., Neukum, G., 2011. Ages and stratigraphy of lunar mare basalts: A synthesis. Geological Society of America Special Papers 477, 1–51. https://doi.org/10.1130/2011.2477(01).

Huang, Q., Xiao, L., Ping, J., Xiao, Z., Qiao, L., Zhao, J., 2013. Density and lithospheric thickness of the Marius Hills shield volcano on the Moon. Scientia Sinica Physica, Mechanica & Astronomica 43, 1395–1402. https://doi.org/10.1360/132013-330.

Huang, Q., Xiao, Z., Xiao, L., 2014. Subsurface structures of large volcanic complexes on the nearside of the Moon: A view from GRAIL gravity. Icarus 243, 48–57. https://doi.org/10.1016/j.icarus.2014.09.009.

Hurwitz, D.M., Head, J.W., Hiesinger, H., 2013. Lunar sinuous rilles: Distribution, characteristics, and implications for their origin. Planet. Space Sci. 79–80, 1–38. https://doi.org/10.1016/j.pss.2012.10.019.

Ivanov, B.A., Melosh, H.J., Pierazzo, E., 2010. Basin-forming impacts: Reconnaissance modeling, in: Geological Society of America Special Papers. Geological Society of America 465, 29–49. https://doi.org/10.1130/2010.2465(03).

Jawin, E.R., Head, J.W., Wilson, L., 2016. Huge pyroclastic cones surrounding Cobra Head, Aristarchus Plateau: Relation to Vallis Schröteri. Lunar and Planet. Sci. 47, abstract #1505.

Jolliff, B.L., Gillis, J.J., Haskin, L.A., Korotev, R.L., Wieczorek, M.A., 2000. Major lunar crustal terranes: Surface expressions and crust-mantle origins. J. Geophys. Res. Planets 105, 4197–4216. https://doi.org/10.1029/1999JE001103.

Jozwiak, L.M., Head, J.W., Neumann, G.A., Wilson, L., 2017. Observational constraints on the identification of shallow lunar magmatism: Insights from floor-fractured craters. Icarus 283, 224–231. https://doi.org/10.1016/j.icarus.2016.04.020.

Jozwiak, L.M., Head, J.W., Wilson, L., 2015. Lunar floor-fractured craters as magmatic intrusions: Geometry, modes of emplacement, associated tectonic and volcanic features, and implications for gravity anomalies. Icarus 248, 424–447. https://doi.org/10.1016/j.icarus.2014.10.052.

Jozwiak, L.M., Head, J.W., Zuber, M.T., Smith, D.E., Neumann, G.A., 2012. Lunar floor-fractured craters: Classification, distribution, origin and implications for magmatism and shallow crustal structure. J. Geophys. Res. 117, E11005. https://doi.org/10.1029/2012JE004134.

Kalynn, J., Johnson, C.L., Osinski, G.R., Barnouin, O., 2013. Topographic characterization of lunar complex craters. Geophys. Res. Lett. 40, 38–42. https://doi.org/10.1029/2012GL053608.

Kiefer, W.S., 2013. Gravity constraints on the subsurface structure of the Marius Hills: The magmatic plumbing of the largest lunar volcanic dome complex. J. Geophys. Res. Planets 118, 733–745. https://doi.org/10.1029/2012JE004111.

Kiefer, W.S., Macke, R.J., Britt, D.T., Irving, A.J., Consolmagno, G.J., 2012. The density and porosity of lunar rocks. Geophys. Res. Lett. 39, L07201. https://doi.org/10.1029/2012GL051319.

Kronrod, V.A., Kuskov, O.L., 2011. Inversion of seismic and gravity data for the composition and core sizes of the Moon. Phys. Solid Earth 47, 711–730. https://doi.org/10.1134/S1069351311070044.

Lawrence, D.J., Feldman, W.C., Barraclough, B.L., Binder, A.B., Elphic, R.C., Maurice, S., Thomsen, D.R., 1998. Global Elemental Maps of the Moon: The Lunar Prospector Gamma-Ray Spectrometer. Science 281, 1484–1489. https://doi.org/10.1126/science.281.5382.1484.

Lawrence, S.J., Stopar, J.D., Hawke, B.R., Greenhagen, B.T., Cahill, J.T.S., Bandfield, J.L., Jolliff, B.L., Denevi, B.W., Robinson, M.S., Glotch, T.D., Bussey, D.B.J., Spudis, P.D., Giguere, T.A., Garry, W.B., 2013. LRO observations of morphology and surface roughness of volcanic cones and lobate lava flows in the Marius Hills. J. Geophys. Res. Planets 118, 615–634. https://doi.org/10.1002/jgre.20060.

Lucchitta, B.K., 1977. Topography, structure, and mare ridges in southern Mare Imbrium and northern Oceanus Procellarum. Proc. Lunar Sci. Conf. 8, 2691-2703.

Marsh, B.D., 1989. Magma Chambers. Annual Review of Earth and Planetary Sciences 17, 439–472. https://doi.org/10.1146/annurev.ea.17.050189.002255.

Melosh, H.J., Freed, A.M., Johnson, B.C., Blair, D.M., Andrews-Hanna, J.C., Neumann, G.A., Phillips, R.J., Smith, D.E., Solomon, S.C., Wieczorek, M.A., Zuber, M.T., 2013. The Origin of Lunar Mascon Basins. Science 340, 1552–1555. https://doi.org/10.1126/science.1235768.

Michaut, C. 2011. Dynamics of magmatic intrusions in the upper crust: Theory and applications to laccoliths on Earth and the Moon. J. Geophys. Res. Solid Earth 116. https://doi.org/10.1029/2010JB008108.

Milbury, C., Johnson, B.C., Melosh, H.J., Collins, G.S., Blair, D.M., Soderblom, J.M., Nimmo, F., Bierson, C.J., Phillips, R.J., Zuber, M.T., 2015. Preimpact porosity controls the gravity signature of lunar craters. Geophys. Res. Lett. 42, 9711–9716. https://doi.org/10.1002/2015GL066198.

Miljković, K., Collins, G.S., Wieczorek, M.A., Johnson, B.C., Soderblom, J.M., Neumann, G.A., Zuber, M.T., 2016. Subsurface morphology and scaling of lunar impact basins. J. Geophys. Res. Planets 121, 1695–1712. https://doi.org/10.1002/2016JE005038.

Miljković, K., Wieczorek, M.A., Collins, G.S., Laneuville, M., Neumann, G.A., Melosh, H.J., Solomon, S.C., Phillips, R.J., Smith, D.E., Zuber, M.T., 2013. Asymmetric Distribution of Lunar Impact Basins Caused by Variations in Target Properties. Science 342, 724–726. https://doi.org/10.1126/science.1243224.

Miljković, K., Wieczorek, M.A., Collins, G.S., Solomon, S.C., Smith, D.E., Zuber, M.T., 2015. Excavation of the lunar mantle by basin-forming impact events on the Moon. Earth and Planet. Sci. Lett. 409, 243–251. https://doi.org/10.1016/j.epsl.2014.10.041.

Moore, H.J., 1965. Geologic map of the Aristarchus region of the Moon (Report No. 465), IMAP. https://doi.org/10.3133/i465.

Mustard, J.F., Pieters, C.M., Isaacson, P.J., Head, J.W., Besse, S., Clark, R.N., Klima, R.L., Petro, N.E., Staid, M.I., Sunshine, J.M., Runyon, C.J., Tompkins, S., 2011. Compositional diversity and geologic insights of the Aristarchus crater from Moon Mineralogy Mapper data. J. Geophys. Res. 116, E00G12. https://doi.org/10.1029/2010JE003726.

Namiki, N., Iwata, T., Matsumoto, K., Hanada, H., Noda, H., Goossens, S., Ogawa, M., Kawano, N., Asari, K., Tsuruta, S., Ishihara, Y., Liu, Q., Kikuchi, F., Ishikawa, T., Sasaki, S., Aoshima, C., Kurosawa, K., Sugita, S., Takano, T., 2009. Farside Gravity Field of the Moon from Four-Way Doppler Measurements of SELENE (Kaguya). Science 323, 900–905. https://doi.org/10.1126/science.1168029.

Neumann, G.A., Goosens, S. Deutsch, A.N., Head, J.W., 2018. Density of lunar mare crust from GRAIL gravity data over young, unflooded craters. AGU Fall Meeting, abstract P31I-1393.

Neumann, G.A., Zuber, M.T., Smith, D.E., Lemoine, F.G., 1996. The lunar crust: Global structure and signature of major basins. J. Geophys. Res. 101, 16841–16863. https://doi.org/10.1029/96JE01246.

Neumann, G.A., Zuber, M.T., Wieczorek, M.A., Head, J.W., Baker, D.M.H., Solomon, S.C., Smith, D.E., Lemoine, F.G., Mazarico, E., Sabaka, T.J., Goossens, S.J., Melosh, H.J., Phillips, R.J., Asmar, S.W., Konopliv, A.S., Williams, J.G., Sori, M.M., Soderblom, J.M., Miljković, K., Andrews-Hanna, J.C., Nimmo, F., Kiefer, W.S., 2015. Lunar impact basins revealed by Gravity Recovery and Interior Laboratory measurements. Science Advances 1, e1500852. https://doi.org/10.1126/sciadv.1500852.

Osinski, G.R., Pierazzo, E. (Eds.), Impact Cratering: Processes and Products, Wiley-Blackwell (2013), pp. 1-20

Parker, R. L., 1972. The rapid calculation of potential anomalies. Geophys. J., 31, 447-455. https://doi.org/10.1111/j.1365-246X.1973.tb06513.x.

Pike, R.J., 1977. Size-dependence in the shape of fresh impact craters on the moon. Roddy, D.J., Pepin, R.O., Merrill R.B. (Eds.), Impact and Explosion Cratering, Pergamon, New York, pp.489–509.

Potter, R.W.K. (2012), Numerical modeling of basin-scale impact crater formation. Ph.D. thesis, Imperial College London, England.

Potter, R.W.K., Kring, D.A., Collins, G.S., 2015. Scaling of basin-sized impacts and the influence of target temperature, in: Geological Society of America Special Papers. Geological Society of America 518, 99–113. https://doi.org/10.1130/2015.2518(06).

Potter, R.W.K., Kring, D.A., Collins, G.S., Kiefer, W.S., McGovern, P.J., 2012. Estimating transient crater size using the crustal annular bulge: Insights from numerical modeling of lunar basin-scale impacts. Geophys. Res. Lett. 39. https://doi.org/10.1029/2012GL052981.

Prettyman, T.H., Hagerty, J.J., Elphic, R.C., Feldman, W.C., Lawrence, D.J., McKinney, G.W., Vaniman, D.T., 2006. Elemental composition of the lunar surface: Analysis of gamma ray spectroscopy data from Lunar Prospector. J. Geophys. Res. Planets 111, E12007. https://doi.org/10.1029/2005JE002656.

Smith, D.E., Zuber, M.T., Neumann, G.A., Lemoine, F.G., Mazarico, E., Torrence, M.H., McGarry, J.F., Rowlands, D.D., Head, J.W., Duxbury, T.H., Aharonson, O., Lucey, P.G., Robinson, M.S., Barnouin, O.S., Cavanaugh, J.F., Sun, X., Liiva, P., Mao, D., Smith, J.C., Bartels, A.E., 2010. Initial observations from the Lunar Orbiter Laser Altimeter (LOLA). Geophys. Res. Lett. 37, L18204. https://doi.org/10.1029/2010GL043751.

Sood, R., Chappaz, L., Melosh, H.J., Howell, K.C., Milbury, C., Blair, D.M., Zuber, M.T., 2017. Detection and characterization of buried lunar craters with GRAIL data. Icarus 289, 157–172. https://doi.org/10.1016/j.icarus.2017.02.013.

Spudis, P.D., 1996. The once and future Moon. Smithsonian Institute Univ. Press, Washington, D.C. 117–118.

Srisutthiyakorn, N., Kiefer, W.S., Kirchoff, M., 2010. Spatial distribution of volcanos in the Marius Hills and comparison with volcanic fields on Earth and Venus. Lunar and Planet. Sci. 41, abstract #1185.

Stadermann, A.C., Zanetti, M.R., Jolliff, B.L., Hiesinger, H., van der Bogert, C.H., Hamilton, C.W., 2018. The age of lunar mare basalts south of the Aristarchus Plateau and effects of secondary craters formed by the Aristarchus event. Icarus 309, 45–60. https://doi.org/10.1016/j.icarus.2018.02.030.

Stopar, J.D., Hawke, B.R., Lawrence, S.J., Robinson, M.S., Giguere, T.A., 2014. Basaltic cones: A relatively common and distinct style of lunar volcanism. Lunar and Planet. Sci. 45, abstract #1425.

Thorey, C., Michaut, C., Wieczorek, M., 2015. Gravitational signatures of lunar floor-fractured craters. Earth and Planet. Sci. Lett. 424, 269–279. https://doi.org/10.1016/j.epsl.2015.04.021.

Trang, D., Gillis-Davis, J.J., Hawke, B.R., 2016. The origin of lunar concentric craters. Icarus 278, 62–78. https://doi.org/10.1016/j.icarus.2016.06.001.

Tye, A.R., Head, J.W., 2013. Mare Tranquillitatis: Distribution of mare domes, relation to broad mare rise, and evidence of a previously unrecognized basin from LOLA altimetric data. Lunar and Planet. Sci., abstract #1319.

Warren, P.H., Wasson, J.T., 1979. The origin of KREEP. Reviews of Geophysics 17, 73–88. https://doi.org/10.1029/RG017i001p00073.

Weitz, C.M., Head, J.W., Pieters, C.M., 1998. Lunar regional dark mantle deposits: Geologic, multispectral, and modeling studies. J. Geophys. Res. Planets 103, 22725–22759. https://doi.org/10.1029/98JE02027.

Wessel, P., Smith, W.H.F., Scharroo, R., Luis, J., Wobbe, F., 2013. Generic Mapping Tools: Improved Version Released. Eos, Transactions American Geophysical Union 94, 409–410. https://doi.org/10.1002/2013EO450001.

Whitford-Stark, J.L., Head, J.W., 1977. The Procellarum volcanic complexes: Contrasting styles of volcanism. Proc. Lunar Sci. Conf. 8, 2705–2724.

Whitford-Stark, J.L., Head, J.W., 1980. Stratigraphy of Oceanus Procellarum basalts: Sources and styles of emplacement. J. Geophys. Res. 85, 6579–6609.

Whitten, J.L., Head, J.W., 2013. Detecting volcanic resurfacing of heavily cratered terrain: Flooding simulations on the Moon using Lunar Orbiter Laser Altimeter (LOLA) data. Planet. Space Sci. 85, 24–37. https://doi.org/10.1016/j.pss.2013.05.013.

Wichman, R.W., Schultz, P.H., 1995. Floor-fractured craters in Mare Smythii and west of Oceanus Procellarum: Implications of crater modification by viscous relaxation and igneous intrusion models. J. Geophys. Res. Planets 100, 21201–21218. https://doi.org/10.1029/95JE02297.

Wieczorek, M.A., Neumann, G.A., Nimmo, F., Kiefer, W.S., Taylor, G.J., Melosh, H.J., Phillips, R.J., Solomon, S.C., Andrews-Hanna, J.C., Asmar, S.W., Konopliv, A.S., Lemoine, F.G., Smith, D.E., Watkins, M.M., Williams, J.G., Zuber, M.T., 2013. The Crust of the Moon as Seen by GRAIL. Science 339, 671–675. https://doi.org/10.1126/science.1231530.

Wieczorek, M.A., Phillips, R.J., 1998. Potential anomalies on a sphere: Applications to the thickness of the lunar crust. J. Geophys. Res. 103, 1715–1724. https://doi.org/10.1029/97JE03136.

Wieczorek, M.A., Phillips, R.J., 2000. The “Procellarum KREEP Terrane”: Implications for mare volcanism and lunar evolution. J. Geophys. Res. 105, 20417–20430. https://doi.org/10.1029/1999JE001092.

Wilson, L., Head, J.W., 2017. Generation, ascent and eruption of magma on the Moon: New insights into source depths, magma supply, intrusions and effusive/explosive eruptions (Part 1: Theory). Icarus 283, 146–175. https://doi.org/10.1016/j.icarus.2015.12.039.

Wilson, L., Head, J.W., 2018. Lunar Floor-Fractured Craters: Modes of Dike and Sill Emplacement and Implications of Gas Production and Intrusion Cooling on Surface Morphology and Structure. Icarus 305, 105–122. https://doi.org/10.1016/j.icarus.2017.12.030.

Wilson, L., Head, J.W., Parfitt, E.A., 2012. The relationship between the height of a volcano and the depth to its magma source zone: A critical reexamination. Geophys. Res. Lett. 19, 1395–1398. https://doi.org/10.1029/92GL01073.

Zhang, F., Zhu, M.-H., Bugiolacchi, R., Huang, Q., Osinski, G.R., Xiao, L., Zou, Y.L., 2017. Diversity of basaltic lunar volcanism associated with buried impact structures: Implications for intrusive and extrusive events. Icarus 307, 216–234. https://doi.org/10.1016/j.icarus.2017.10.039.

Zhang, F., Zhu, M.-H., Zou, Y.L., 2016. Late stage Imbrium volcanism on the Moon: Evidence for two source regions and implications for the thermal history of Mare Imbrium. Earth and Planet. Sci. Lett. 445, 13–27. https://doi.org/10.1016/j.epsl.2016.04.003.

Zisk, S.H., Hodges, C.A., Moore, H.J., Shorthill, R.W., Thompson, T.W., Whitaker, E.A., Wilhelms, D.E., 1977. The Aristarchus-Harbinger region of the moon: Surface geology and history from recent remote-sensing observations. The Moon 17, 59–99. https://doi.org/10.1007/BF00566853.

Zuber, M.T., Smith, D.E., Lehman, D.H., Hoffman, T.L., Asmar, S.W., Watkins, M.M., 2013b. Gravity Recovery and Interior Laboratory (GRAIL): Mapping the Lunar Interior from Crust to Core. Space Sci. Rev. 178, 3–24. https://doi.org/10.1007/s11214-012-9952-7.

Zuber, M.T., Smith, D.E., Neumann, G.A., Goossens, S., Andrews-Hanna, J.C., Head, J.W., Kiefer, W.S., Asmar, S.W., Konopliv, A.S., Lemoine, F.G., Matsuyama, I., Melosh, H.J., McGovern, P.J., Nimmo, F., Phillips, R.J., Solomon, S.C., Taylor, G.J., Watkins, M.M., Wieczorek, M.A., Williams, J.G., Jansen, J.C., Johnson, B.C., Keane, J.T., Mazarico, E., Miljković, K., Park, R.S., Soderblom, J.M., Yuan, D.-N., 2016. Gravity field of the

Orientale basin from the Gravity Recovery and Interior Laboratory Mission. Science 354, 438–441. https://doi.org/10.1126/science.aag0519.

Zuber, M.T., Smith, D.E., Watkins, M.M., Asmar, S.W., Konopliv, A.S., Lemoine, F.G., Melosh, H.J., Neumann, G.A., Phillips, R.J., Solomon, S.C., Wieczorek, M.A., Williams, J.G., Goossens, S.J., Kruizinga, G., Mazarico, E., Park, R.S., Yuan, D.-N., 2013a. Gravity Field of the Moon from the Gravity Recovery and Interior Laboratory (GRAIL) Mission. Science 339, 668–671. https://doi.org/10.1126/science.1231507.

Tables

Table 1. Model parameters.

		Southeast Aristarchus	*Northern Marius Hills*	*Southern Marius Hills*	*Northern Flamsteed*
Center latitude (°N)		21.4	14.0	8.3	0.8
Center longitude (°E)		311.8	307.25	308.6	316.4
Estimated PBGA diameter (km)		100	90	120	190
Bouguer gravity peak (mGal)		166	145	140	178
Estimated crustal thickness (km) (Wieczorek et al., 2013)		16	18	17	14
Buried craters (**MODEL 1**)	Series of vertically stacked crater-fill cylindrical disks	3.51-km thick; 96-, 84-, 72-, and 60-km wide	3.44-km thick; 90-, 78-, 66-. and 54-km wide	3.58-km thick; 106-, 92-, 78-, and 64-km wide	3.98-km thick; 188-, 168-, 148-, and 128-km wide
	Rim height (km)	1.458	1.421	1.517	1.907
	Fill volume (km^3)	17059	14472	20953	79467
	Bouguer gravity peak estimated from model (mGal) for crust = 2800 kg/m^3	Mare fill: 44.4 Total anomaly: 44.4	Mare fill: 42.2 Total anomaly: 42.2	Mare fill: 44.9 Total anomaly: 44.9	Mare fill: 54.7 Total anomaly: 54.7
	Bouguer gravity peak estimated from model (mGal) for crust = 2500 kg/m^3	Mare fill: 82.5 Total anomaly: 82.5	Mare fill: 78.4 Total anomaly: 78.4	Mare fill: 83.5 Total anomaly: 83.5	Mare fill: 101.6 Total anomaly: 101.6
Buried craters + mantle upwelling (**MODEL 2**)	Mare (3150 kg/m^3) fill parameters	Cylindrical disks as in Case 1			
	Series of vertically stacked mantle uplift cylinders	6.4-km thick; 70-, 60-, and 50-km wide	5.6-km thick; 78-, 68-, and 58-km wide	5.95-km thick; 106-, 84-, and 64-km wide	7.2-km thick; 150-, 130-, 110-, and 90-km wide
	Mantle (3400 kg\m^3) volume (km^3)	18040	20120	35030	79450
	Bouguer gravity peak estimated from model (mGal) for crust = 2800 kg/m^3	Mare fill: 44.4 Mantle uplift: 86.4 Total anomaly: 130.8	Mare fill: 42.2 Mantle uplift: 79.9 Total anomaly: 122.1	Mare fill: 44.9 Mantle uplift: 95.7 Total anomaly: 140.6	Mare fill: 54.7 Mantle uplift: 133.7 Total anomaly: 188.4
	Bouguer gravity peak estimated from model (mGal) for crust = 2500 kg/m^3	Mare fill: 82.5 Mantle uplift: 129.6 Total anomaly: 212.1	Mare fill: 78.4 Mantle uplift: 119.8 Total anomaly: 198.2	Mare fill: 83.5 Mantle uplift: 143.5 Total anomaly: 227.0	Mare fill: 101.6 Mantle uplift: 200.5 Total anomaly: 302.1
Buried craters + sill (**MODEL 3**)	Mare (3150 kg/m^3) fill parameters	Cylindrical disks as in Case 1			
	Sill (8 km depth, 2 km thickness) diameter (km)	60	60	60	130
	Sill volume (km^3)	5670	5670	5670	26500
	Bouguer gravity peak estimated from model (mGal) for	Mare fill: 44.4 Sill intrusion: 21.1	Mare fill: 42.2 Sill intrusion: 20.9	Mare fill: 44.9 Sill intrusion: 20.9	Mare fill: 54.7 Sill intrusion: 25.2

	crust = 2800 kg/m^3, sill = 3150 kg/m^3	Total anomaly: 65.5	Total anomaly: 63.1	Total anomaly: 65.8	Total anomaly: 79.9
	Bouguer gravity peak estimated from model (mGal) for crust = 2500 kg/m^3, sill = 3150 kg/m^3	Mare fill: 82.5 Sill intrusion: 39.2 Total anomaly: 121.7	Mare fill: 78.4 Sill intrusion: 38.9 Total anomaly: 117.3	Mare fill: 83.5 Sill intrusion: 38.8 Total anomaly: 122.3	Mare fill: 101.6 Sill intrusion: 46.9 Total anomaly: 148.5
	Bouguer gravity peak estimated from model (mGal) for crust = 2800 kg/m^3, sill = 3400 kg/m^3	Mare fill: 44.4 Sill intrusion: 36.2 Total anomaly: 80.6	Mare fill: 42.2 Sill intrusion: 35.9 Total anomaly: 78.1	Mare fill: 44.9 Sill intrusion: 35.8 Total anomaly: 80.7	Mare fill: 54.7 Sill intrusion: 43.3 Total anomaly: 98.0
	Bouguer gravity peak estimated from model (mGal) for crust = 2500 kg/m^3, sill = 3400 kg/m^3	Mare fill: 82.5 Sill intrusion: 54.2 Total anomaly: 136.7	Mare fill: 78.4 Sill intrusion: 53.8 Total anomaly: 132.3	Mare fill: 83.5 Sill intrusion: 53.7 Total anomaly: 137.2	Mare fill: 101.6 Sill intrusion: 64.9 Total anomaly: 166.5
Buried craters + vertical dike swarm (**MODEL 4**)	Mare (3150 kg/m^3) fill parameters	Cylindrical disks as in Case 1			
	1 cylinder representing linear combination of all vertical dikes	12-km thick; 56-km wide	12-km thick; 52-km wide	12-km thick; 64-km wide	12-km thick; 128-km wide
	Density of dike swarm (kg/m^3)	3400	3400	3400	3400
	Crust occupied by dike swarm (%)	50	50	50	50
	Bouguer gravity peak estimated from model (mGal) for crust = 2800 kg/m^3	Mare fill: 44.4 Dike swarm: 89.5 Total anomaly: 133.9	Mare fill: 42.2 Dike swarm: 84.7 Total anomaly: 126.9	Mare fill: 44.9 Dike swarm: 94.6 Total anomaly: 139.5	Mare fill: 54.7 Dike swarm: 113.1 Total anomaly: 167.8
	Bouguer gravity peak estimated from model (mGal) for crust = 2500 kg/m^3	Mare fill: 82.5 Dike swarm: 134.2 Total anomaly: 216.7	Mare fill: 78.4 Dike swarm: 127.1 Total anomaly: 205.5	Mare fill: 83.5 Dike swarm: 141.9 Total anomaly: 225.4	Mare fill: 101.6 Dike swarm: 170.6 Total anomaly: 272.2
Sill with no buried crater (**MODEL 5**)	Sill (8 km depth; 2 km thickness) diameter (km)	60	60	60	130
	Sill volume (km^3)	5670	5670	5670	26500
	Bouguer gravity peak estimated from model (mGal) for crust = 2800 kg/m^3, sill = 3150 kg/m^3	Sill intrusion: 21.1 Total anomaly: 21.1	Sill intrusion: 20.9 Total anomaly: 20.9	Sill intrusion: 20.9 Total anomaly: 20.9	Sill intrusion: 25.2 Total anomaly: 25.2
	Bouguer gravity peak estimated from model (mGal) for crust = 2500 kg/m^3, sill = 3150 kg/m^3	Sill intrusion: 39.2 Total anomaly: 39.2	Sill intrusion: 38.9 Total anomaly: 38.9	Sill intrusion: 38.8 Total anomaly: 38.8	Sill intrusion: 46.9 Total anomaly: 46.9
	Bouguer gravity peak estimated from	Sill intrusion: 36.2	Sill intrusion: 35.9	Sill intrusion: 35.8	Sill intrusion: 43.3

	model (mGal) for crust = 2800 kg/m^3, sill = 3400 kg/m^3	Total anomaly: 36.2	Total anomaly: 35.9	Total anomaly: 35.8	Total anomaly: 43.3
	Bouguer gravity peak estimated from model (mGal) for crust = 2500 kg/m^3, sill = 3400 kg/m^3	Sill intrusion: 54.2 Total anomaly: 54.2	Sill intrusion: 53.8 Total anomaly: 53.8	Sill intrusion: 53.7 Total anomaly: 53.7	Sill intrusion: 64.9 Total anomaly: 64.9
Vertical dike swarm with no buried crater (**MODEL 6**)	1 cylinder representing linear combination of all vertical dikes	17.4-km thick; 56-km wide	18.5-km thick; 52-km wide	17.5-km thick; 64-km wide	17.5-km thick; 128-km wide
	Density of dike swarm (kg/m^3)	3400	3400	3400	3400
	Crust occupied by dike swarm (%)	37–50	37–50	37–50	37–50
	Bouguer gravity peak estimated from model (mGal) for crust = 2800 kg/m^3, dikes = 37%	Dike swarm: 108.4 Total anomaly: 108.4	Dike swarm: 114.3 Total anomaly: 114.3	Dike swarm: 114.0 Total anomaly: 114.0	Dike swarm: 135.6 Total anomaly: 135.6
	Bouguer gravity peak estimated from model (mGal) for crust = 2500 kg/m^3, dikes = 37%	Dike swarm: 162.7 Total anomaly: 162.7	Dike swarm: 171.4 Total anomaly: 171.4	Dike swarm: 170.9 Total anomaly: 170.9	Dike swarm: 203.4 Total anomaly: 203.4
	Bouguer gravity peak estimated from model (mGal) for crust = 2800 kg/m^3, dikes = 50%	Dike swarm: 146.5 Total anomaly: 146.5	Dike swarm: 154.4 Total anomaly: 154.4	Dike swarm: 154.0 Total anomaly: 154.0	Dike swarm: 183.2 Total anomaly: 183.2
	Bouguer gravity peak estimated from model (mGal) for crust = 2500 kg/m^3, dikes = 50%	Dike swarm: 219.8 Total anomaly: 219.8	Dike swarm: 231.6 Total anomaly: 231.6	Dike swarm: 231.0 Total anomaly: 231.0	Dike swarm: 274.8 Total anomaly: 274.8

Table 2. Characteristics consistent with ancient impact craters for each positive Bouguer gravity anomaly (PBGA).

PBGA	Gravity anomaly	Topography	Other
Southern AP	Quasi-circular in shape	Partial rim crest; Low in center	Consistent with [1]buried crater database
Northern Marius Hills	Quasi-circular in shape		Linear rilles/graben along PBGA[2]; Consistent with [1]buried crater database
Southern Marius Hills	Quasi-circular in shape	Low in center	Discontinuous ring of hills[2], Consistent with [1]buried crater database
Northern Flamsteed	Quasi-circular in shape		Crustal thickness signature[3]; Consistent with [1]buried crater database

[1]Evans et al. (2016); [2]Zhang et al. (2017); [3]Frey (2011)

Figures

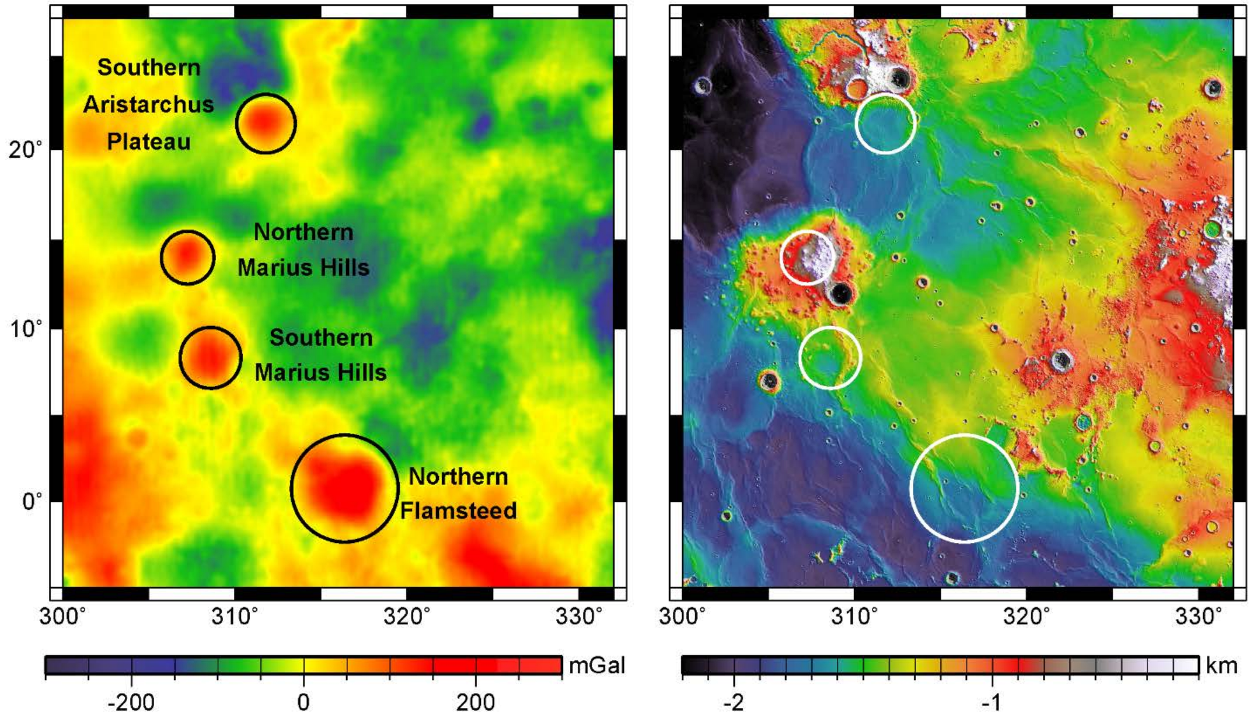

Fig. 1. Four positive Bouguer gravity anomalies in Oceanus Procellarum. GRAIL-derived Bouguer spherical harmonic solution to degree 6-660 is displayed on the left, with an assumed density correction of 2800 kg/m^3, windowed from a global, locally patched, constrained solution (GRGM1200B_RM1_1E1; Goossens et al., 2018). Surface elevations, measured from the LOLA instrument (Smith et al., 2010), are shown on the right.

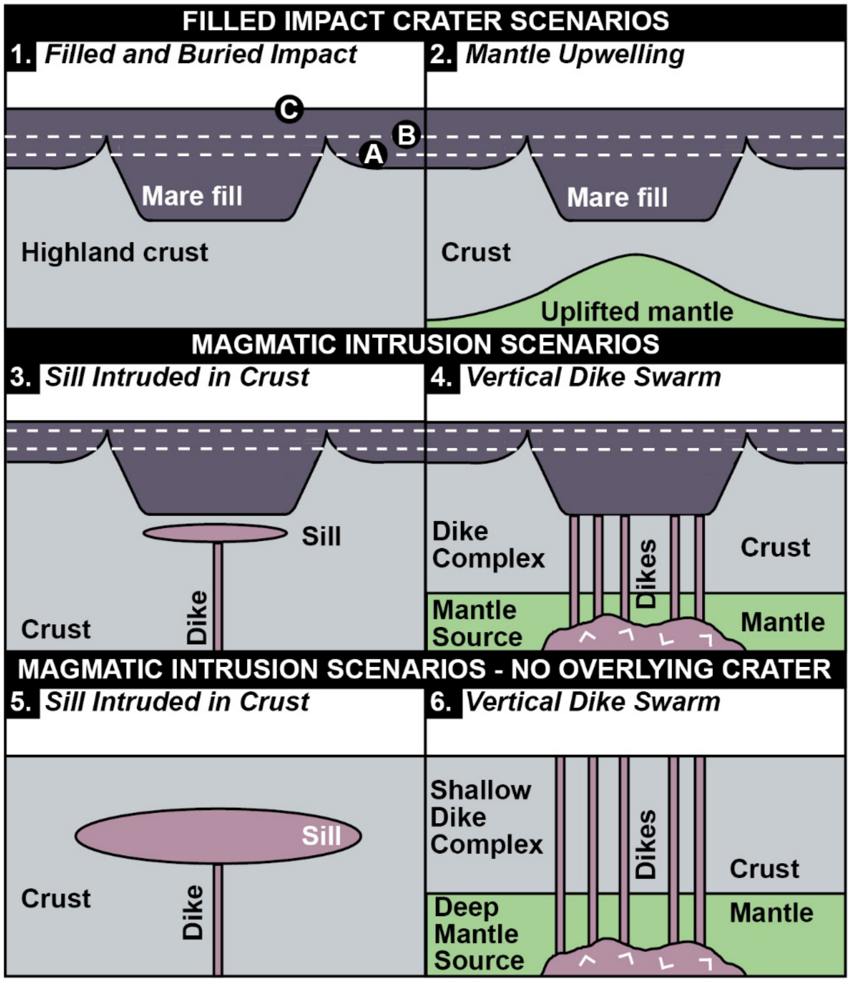

Fig. 2. Interpretive endmember scenarios. Models 1–2 are variations of filled craters, which are associated with (A) identifiable crater rim crests when filled below the rim, (B) wrinkle ridges when flooded to the rim crest, or (C) no topographic expression when flooded over. Models 3–4 are variations of magmatic intrusions. Models 5–6 are variations of magmatic intrusions that are not superposed by mare-filled impact craters. Schematics are not to scale.

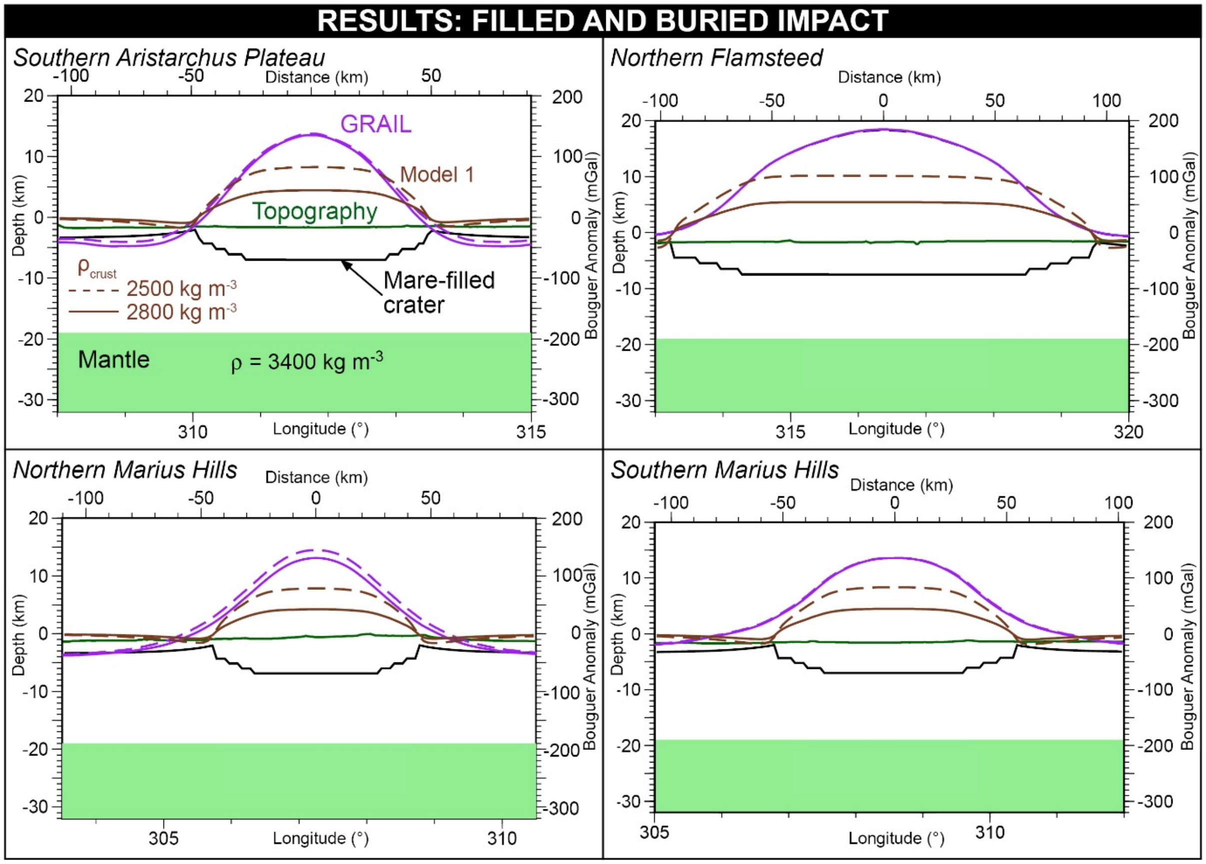

Fig. 3. East-west profiles of modeling results for each PBGA for Model 1 (**Fig. 2.1**), where anomalies represent filled and buried impact craters. Here, modeled PBGAs are due to the density contrast between dense mare material (3150 kg/m^3) and the underlying crust. The model results are plotted in solid brown for a density contrast of 350 kg/m^3 and dashed brown for a density contrast of 650 kg/m^3. Azimuthally averaged profiles of the GRAIL-derived Bouguer anomalies are plotted in solid and dashed purple lines for a crustal density of 2800 kg/m^3 and 2500 kg/m^3, respectively. LOLA-measured surface topographies are plotted in dark green and filled impact craters are plotted in black. The results are shown with a vertical exaggeration of 2.5:1.

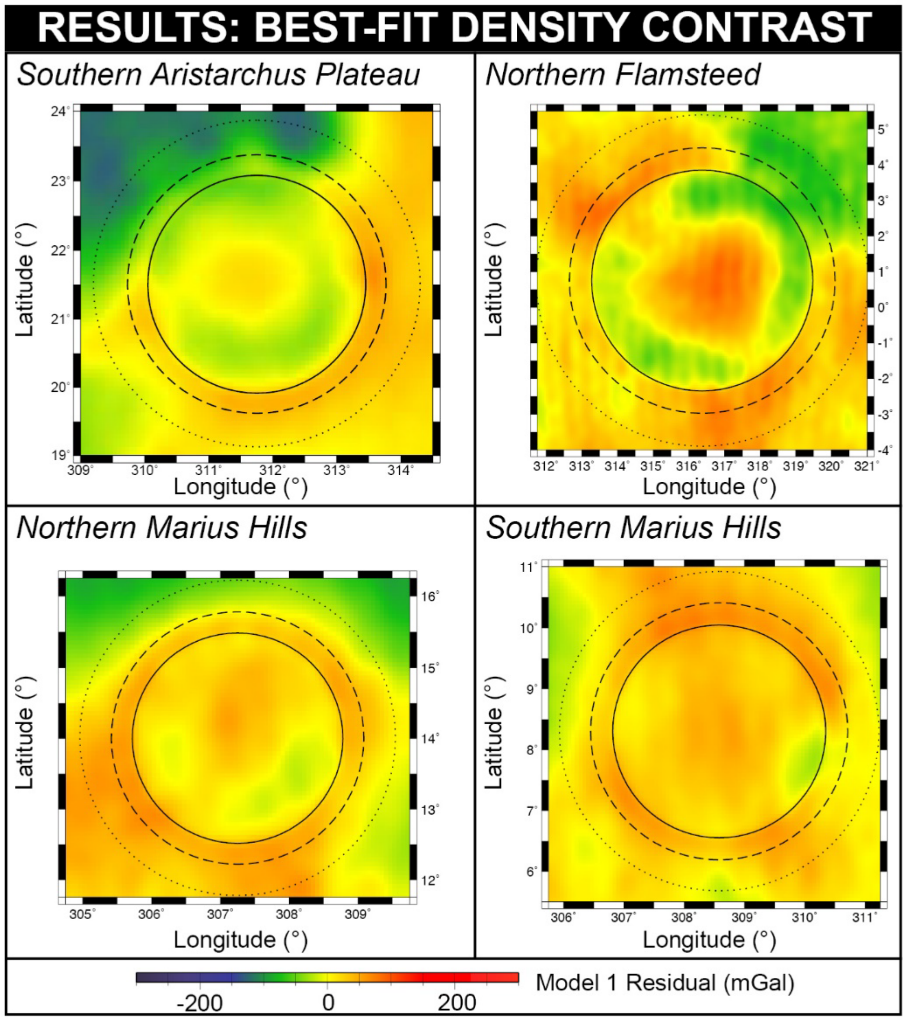

Fig. 4. Residual plots solving for the best-fit densities for the individual PBGAs for Model 1 (**Fig. 2.1**), averaged over 1.5R, where R is the radius of the anomaly. The best-fit density between the crust and mare is 1100 kg/m^3 for *Southern AP*, 960 kg/m^3 for *Northern Marius Hills*, 810 kg/m^3 for *Southern Marius Hills*, and 730 kg/m^3 for *Northern Flamsteed.*

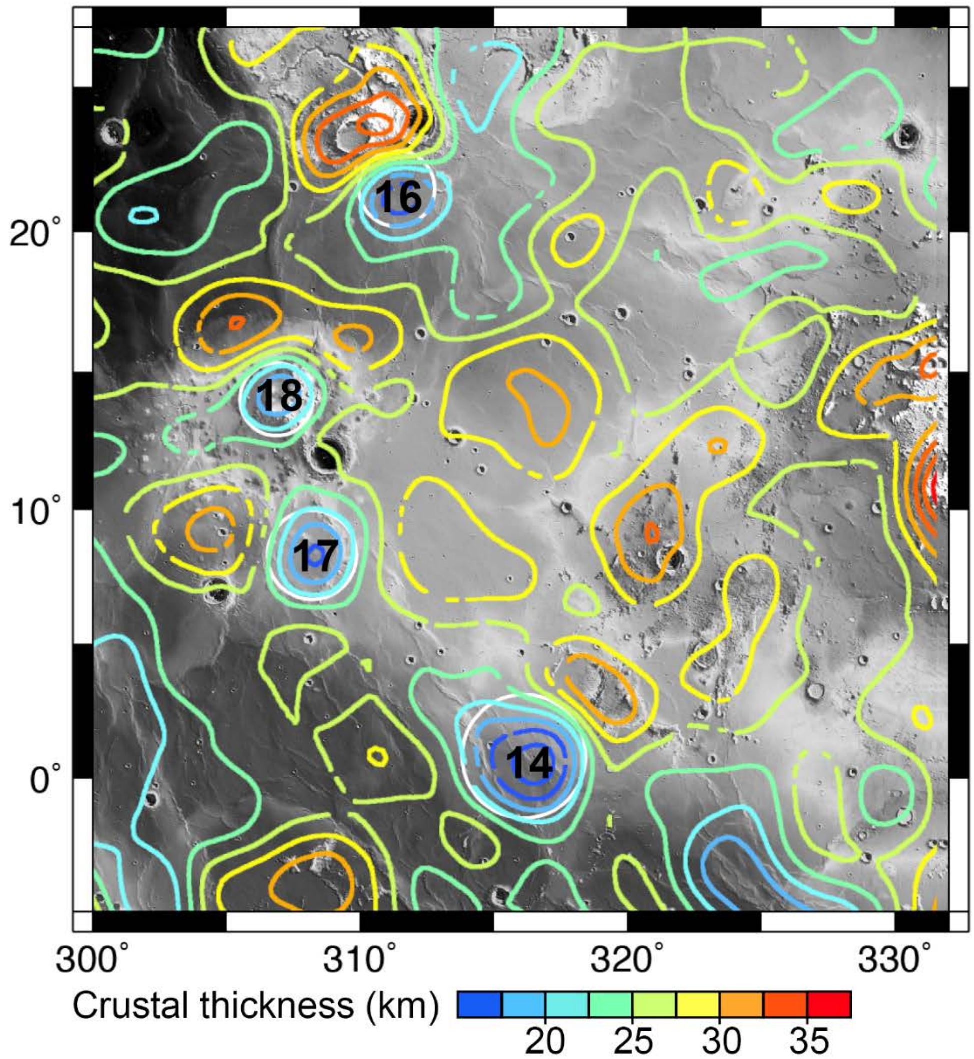

Fig. 5. Crustal thickness contours (2.5-km increments) are plotted for the region of study on top of LOLA-measured surface topography. Contours represent crustal thickness results of Model 1 from Wieczorek et al. (2013), derived from GRAIL gravity data model GL0420A. The assumed crustal porosity in this model is 12%, and the mantle density is 3220 kg/m^3 (Wieczorek et al., 2013).

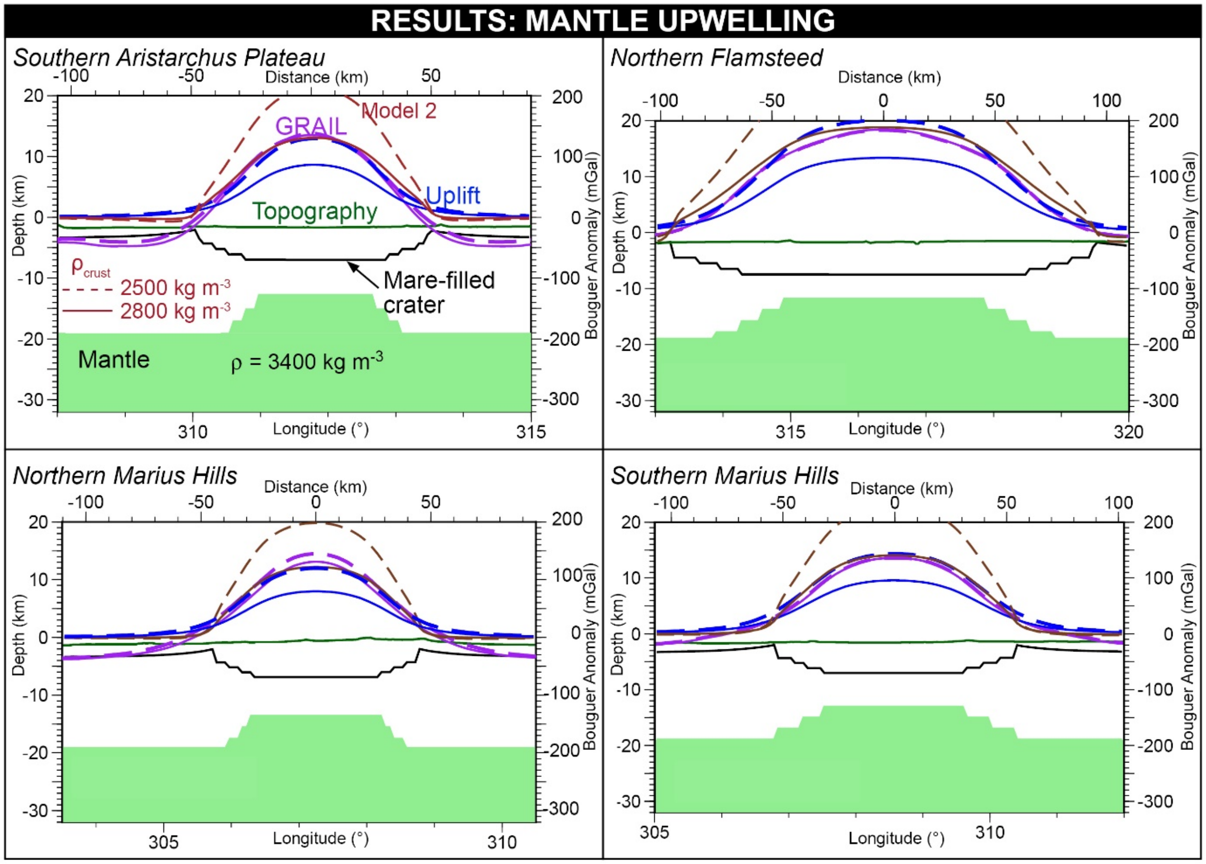

Fig. 6. East-west profiles of modeling results for each PBGA for Model 2 (**Fig. 2.2**), where anomalies represent filled and buried impact craters associated with mantle upwelling. Here, modeled PBGAs are due to the density contrast between dense mare material (3150 kg/m^3) flooded within a crater, the uplift of dense mantle material (3400 kg/m^3), and the crust. The model results are plotted in solid brown for a crustal density of 2800 kg/m^3 and dashed brown for a crustal density of 2500 kg/m^3. The gravitational attraction of the uplifted mantle is plotted in solid blue for a crustal density of 2800 kg/m^3 and dashed blue for a crustal density of 2500 kg/m^3. Azimuthally averaged profiles of the GRAIL-derived Bouguer anomalies are plotted in solid and dashed purple lines for a crustal density of 2800 kg/m^3 and 2500 kg/m^3, respectively. Filled impact craters are represented by black lines, mantle upwelling is represented by the filled green polygons, and the LOLA-measured surface topographies are plotted in dark green. The results are shown with a vertical exaggeration of 2.5:1.

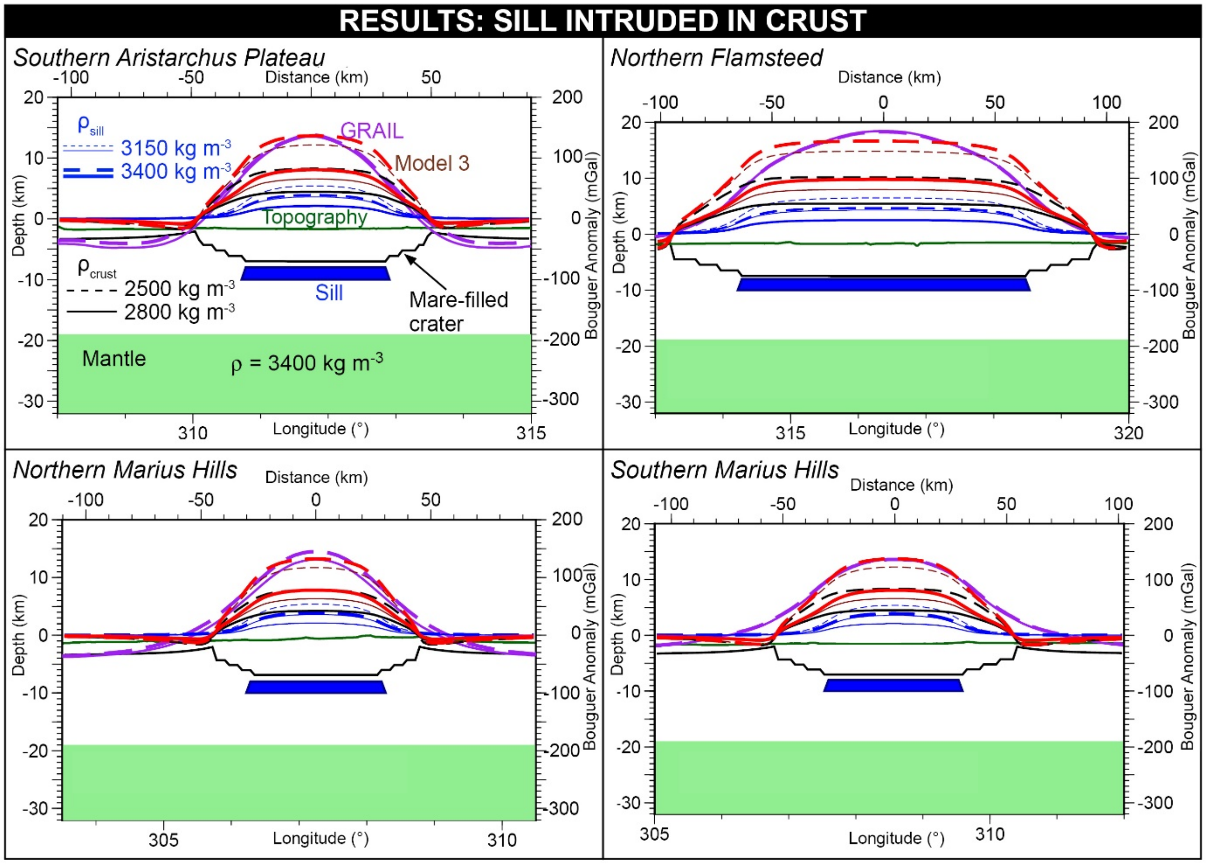

Fig. 7. East-west profiles of modeling results for each PBGA for Model 3 (**Fig. 2.3**), where anomalies represent sills intruded in the shallow subsurface beneath filled and buried impact craters. Here, modeled PBGAs are due to the density contrast between dense mare material (3150 kg/m^3), the intrusion of a 2-km thick dense sill, and the crust. The gravitational attraction of sill with a density 3150 kg/m^3 (thinner lines) and 3400 kg/m^3 (thicker lines) are shown for a crustal density of both 2500 kg/m^3 (dashed lines) and 2800 kg/m^3 (solid lines). The model results for a 3150 kg/m^3 sill are plotted in solid brown for a crustal density of 2800 kg/m^3 and dashed brown for a crustal density of 2500 kg/m^3. The model results for a 3400 kg/m^3 sill are plotted in solid red for a crustal density of 2800 kg/m^3 and dashed red for a crustal density of 2500 kg/m^3. The gravitational attraction of the filled crater is plotted in solid black for a crustal density of 2800 kg/m^3 and dashed black for a crustal density of 2500 kg/m^3. Azimuthally averaged profiles of the GRAIL-derived Bouguer anomalies are plotted in solid and dashed purple lines for a crustal density of 2800 kg/m^3 and 2500 kg/m^3, respectively. Filled impact craters are represented by black lines, intruded sills are represented by the filled blue polygons, and the LOLA-measured surface topographies are plotted in dark green. The results are shown with a vertical exaggeration of 2.5:1.

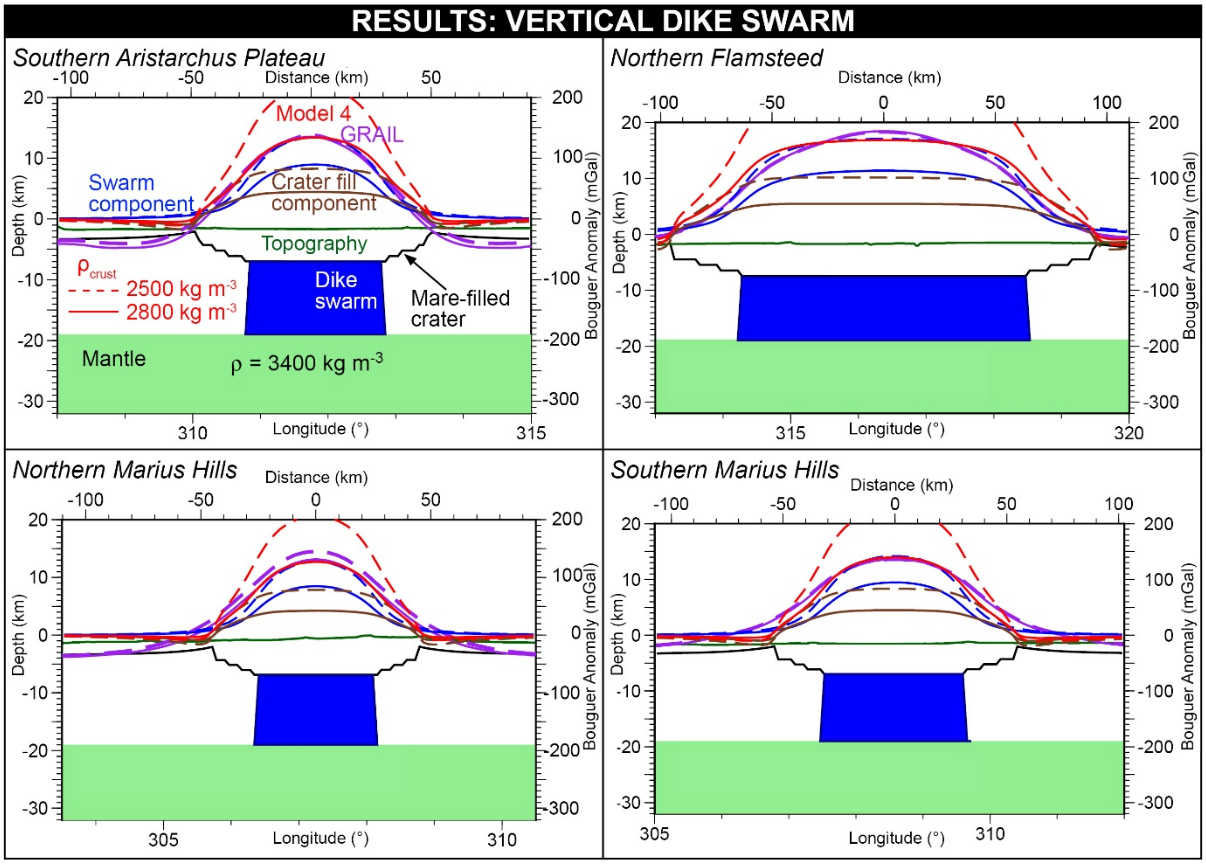

Fig. 8. East-west profiles of modeling results for each PBGA for Model 4 (**Fig. 2.4**), where anomalies represent subsurface vertical dike swarms fed by a deep mantle source, concentrated beneath filled impact craters. Here, modeled PBGAs are due to the density contrast between the crust and vertical dike swarms (3150 kg/m^3) that extend from the crust-mantle boundary to the floors of filled craters and occupy 50% of the crust. The model results are plotted in solid red for a crustal density of 2800 kg/m^3 and dashed red for a crustal density of 2500 kg/m^3. The gravitational attraction of the dike swarm is plotted in solid blue for a crustal density of 2800 kg/m^3 and dashed blue for a crustal density of 2500 kg/m^3. The gravitational attraction of the filled crater is plotted in solid brown for a crustal density of 2800 kg/m^3 and dashed brown for a crustal density of 2500 kg/m^3. Azimuthally averaged profiles of the GRAIL-derived Bouguer anomalies are plotted in solid and dashed purple lines for a crustal density of 2800 kg/m^3 and 2500 kg/m^3, respectively. Filled impact craters are represented by black lines, the vertical dike swarms are represented by the solid blue rectangles, and the LOLA-measured surface topographies are plotted in green. The results are shown with a vertical exaggeration of 2.5:1.

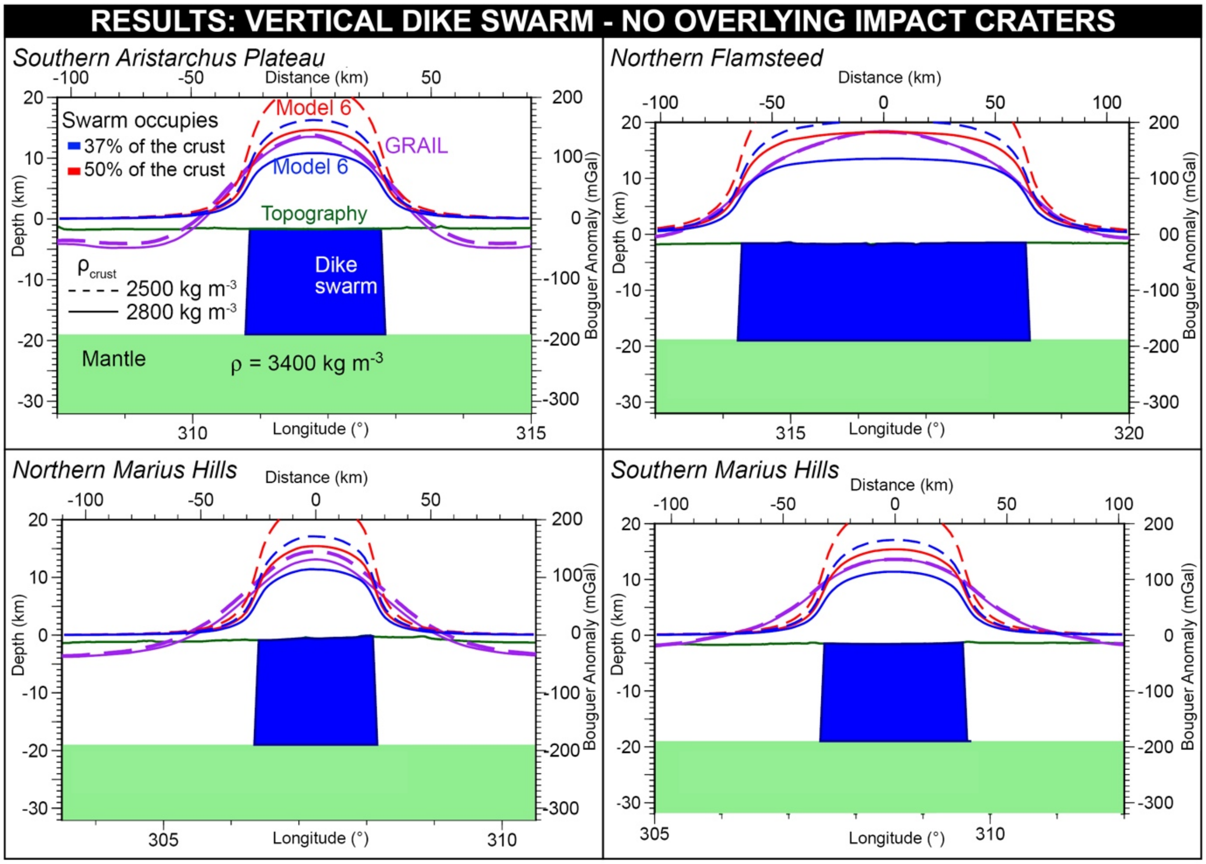

Fig. 9. East-west profiles of modeling results for each PBGA for Model 6 (**Fig. 2.6**), where anomalies represent subsurface vertical dike swarms fed by a deep mantle source, and where the anomalies are not located beneath filled impact craters. Here, the modeled PBGAs are due to the density contrast between the crust and vertical dike swarms that extend from the crust-mantle boundary to the surface, and occupy 37% (blue lines) and 50% (red lines) of the crust. The model results are plotted in solid for a crustal density of 2800 kg/m^3 and dashed for a crustal density of 2500 kg/m^3. The gravitational attraction of the dike swarm is plotted in solid blue for a crustal density of 2800 kg/m^3 and dashed blue for a crustal density of 2500 kg/m^3. Azimuthally averaged profiles of the GRAIL-derived Bouguer anomalies are plotted in solid and dashed purple lines for a crustal density of 2800 kg/m^3 and 2500 kg/m^3, respectively. Dike swarms are represented by the filled blue polygons and the LOLA-measured surface topographies are plotted in green. The results are shown with a vertical exaggeration of 2.5:1.

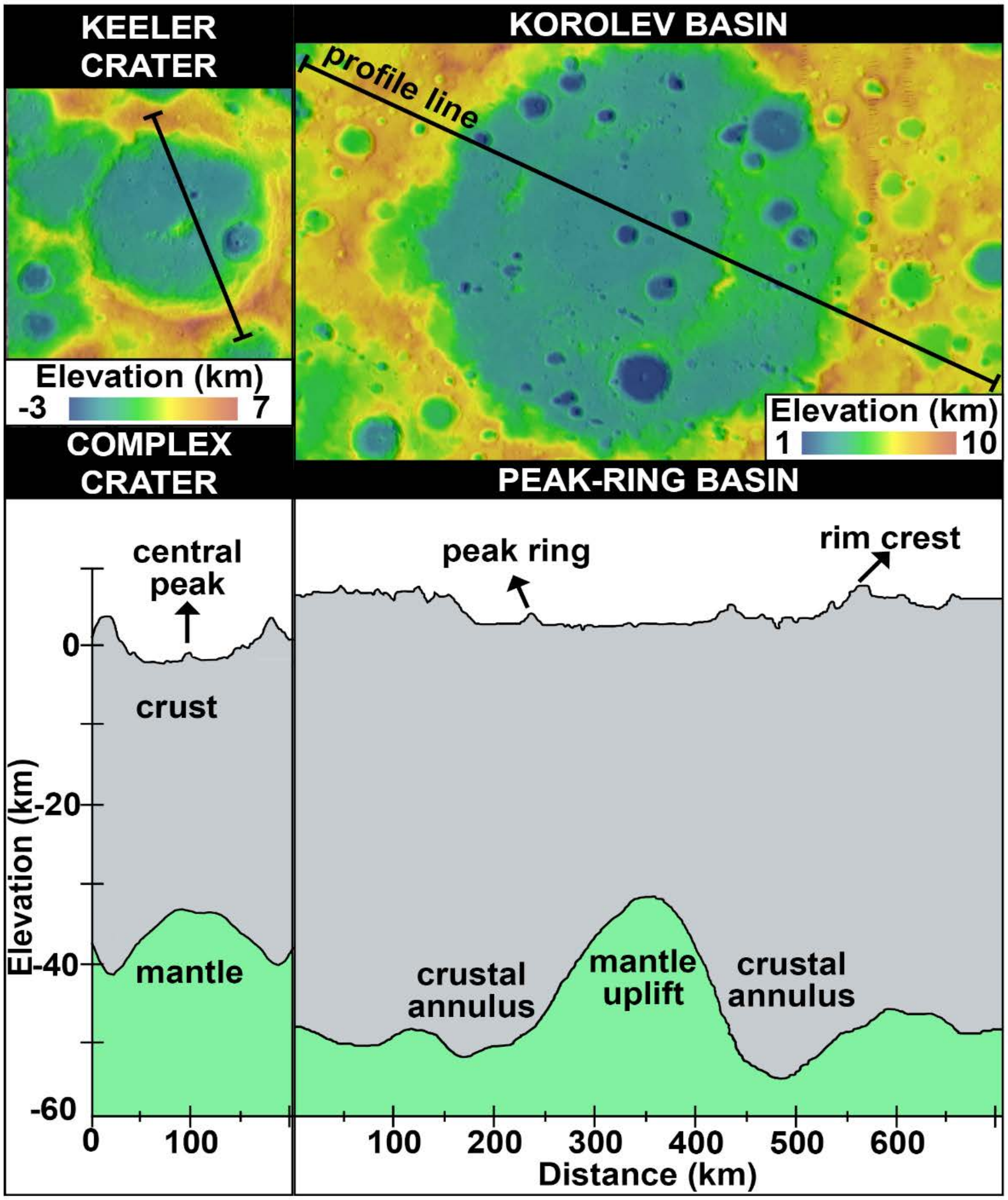

Fig. 10. Comparison of complex craters and peak-ring basins. Top: LOLA-topography of Keeler crater (9.7°S, 162.0°E; 161 km diameter) and Korolev basin (4.0°S, 157.4°E; 437 km diameter). Bottom: Profile plots of the LOLA-measured surface topographies and the estimated crust-mantle interface depth (Wieczorek et al., 2013) for both Keeler (left) and Korolev (right). Complex craters on the Moon typically have a depth-to-diameter ratio of ~0.03, while peak-ring basins have a smaller ratio of ~0.01 (Baker et al., 2012). Baker et al. (2017) show that complex craters are associated with irregular, minor deviations from the pre-impact crust-mantle boundary. Peak-ring basins are associated with crustal annuli surrounding mantle uplift, creating the distinctive PBGA within the peak ring, which is surrounded by a negative Bouguer gravity ring interpreted to be thickened crust.